Article

Transport and inhibition mechanisms of the human noradrenaline transporter

Tuo Hu[1,2,3,9], Zhuoya Yu[1,2,3,9], Jun Zhao[4,9], Yufei Meng[1,2,3], Kristine Salomon[5], Qinru Bai[1,2,3], Yiqing Wei[1,2,3], Jinghui Zhang[6], Shujing Xu[7], Qiuyun Dai[7], Rilei Yu[6], Bei Yang[1], Claus J. Loland[5✉] & Yan Zhao[1,8✉]

The noradrenaline transporter (also known as norepinephrine transporter) (NET) has a critical role in terminating noradrenergic transmission by utilizing sodium and chloride gradients to drive the reuptake of noradrenaline (also known as norepinephrine) into presynaptic neurons[1–3]. It is a pharmacological target for various antidepressants and analgesic drugs[4,5]. Despite decades of research, its structure and the molecular mechanisms underpinning noradrenaline transport, coupling to ion gradients and non-competitive inhibition remain unknown. Here we present high-resolution complex structures of NET in two fundamental conformations: in the apo state, and bound to the substrate noradrenaline, an analogue of the χ-conotoxin MrlA (χ-MrlA[EM]), bupropion or ziprasidone. The noradrenaline-bound structure clearly demonstrates the binding modes of noradrenaline. The coordination of Na^{+} and Cl^{−} undergoes notable alterations during conformational changes. Analysis of the structure of NET bound to χ-MrlA[EM] provides insight into how conotoxin binds allosterically and inhibits NET. Additionally, bupropion and ziprasidone stabilize NET in its inward-facing state, but they have distinct binding pockets. These structures define the mechanisms governing neurotransmitter transport and non-competitive inhibition in NET, providing a blueprint for future drug design.

Noradrenaline has a crucial role as a neurotransmitter in the central and peripheral nervous systems[1]. The noradrenergic pathway contributes significantly to the regulation of essential functions such as pain perception, sleep–wake cycle, arousal, attention, feeding behaviour and the fight-or-flight responses[6–10]. NET has an indispensable role in terminating the action of noradrenaline in the synapse by taking up released noradrenaline back into the presynaptic terminal[2,3]. NET is one of three monoamine transporters (MATs) expressed in humans—a group of proteins that includes the sodium-dependent serotonin transporter (SERT) and the sodium-dependent dopamine transporter (DAT). MATs belong to the SLC6 family of secondary active transporters that utilize a Na^{+} gradient to couple 'downhill' transport of Na^{+} with 'uphill' transport of substrate across the plasma membrane. Accumulating evidence implicates NET in various neuropsychiatric disorders, such as depression, attention deficit hyperactivity disorder and pain[11–13].

Despite advances in structural investigations into human SERT and *Drosophila* DAT[14–20], fundamental questions remain regarding the transport mechanism of NET, such as ligand recognition, ion-binding sites and the conformational changes that occur between distinct functional states. Further, the χ-conotoxin MrlA (χ-MrlA) is a potent and highly selective allosteric inhibitor of NET[21–23], and the χ-MrlA analogue

XEN2174 has progressed to phase II clinical trials for the treatment of neuropathic pain[5]. However, the binding site and selectivity of this conopeptide remain largely unexplored. Stabilizing MATs in their inward-facing conformation potentially results in unique pharmacological responses, as indicated by studies showing that phosphorylation of MATs is increased in their inward-facing conformational state, which regulates their expression, activity, trafficking and degradation[24,25]. Therefore, the inhibition mechanism of MATs in their inward-facing conformation with drugs is a critical and compelling target for clinicians. Bupropion is the only clinically approved selective noradrenaline and dopamine reuptake inhibitor available for the treatment of depression[26]. Additionally, an increasing number of disease-associated, folding-deficient mutants of NET and DAT have been identified[27–29], and bupropion has been recognized as an effective pharmacological chaperone for rescuing these misfolded mutants[30]. The mechanisms underlying its binding mode to NET, its inhibitory effects and its unique binding specificity among MATs have yet to be fully investigated.

Here we report single-particle cryo-electron microscopy (cryo-EM) structures of NET in the apo state and in the presence of the substrate noradrenaline, an analogue of the analgesic χ-MrlA, bupropion and ziprasidone. Combined with functional assays, our study provides

[1]National Laboratory of Biomacromolecules, CAS Center for Excellence in Biomacromolecules, Institute of Biophysics, Chinese Academy of Sciences, Beijing, China. [2]State Key Laboratory of Brain and Cognitive Science, Institute of Biophysics, Chinese Academy of Sciences, Beijing, China. [3]College of Life Sciences, University of Chinese Academy of Sciences, Beijing, China. [4]Peking University Institute of Advanced Agricultural Sciences, Shandong Laboratory of Advanced Agricultural Sciences at Weifang, Weifang, China. [5]Laboratory for Membrane Protein Dynamics, Department of Neuroscience, Faculty of Health and Medical Sciences, University of Copenhagen, Copenhagen, Denmark. [6]Key Laboratory of Marine Drugs, Chinese Ministry of Education, School of Medicine and Pharmacy, Ocean University of China, Qingdao, China. [7]Beijing Institute of Biotechnology, Beijing, China. [8]Beijing Key Laboratory of Mental Disorders, National Clinical Research Center for Mental Disorders & National Center for Mental Disorders, Beijing Anding Hospital, Capital Medical University, Beijing, China. [9]These authors contributed equally: Tuo Hu, Zhuoya Yu, Jun Zhao. ✉e-mail: cllo@sund.ku.dk; zhaoy@ibp.ac.cn
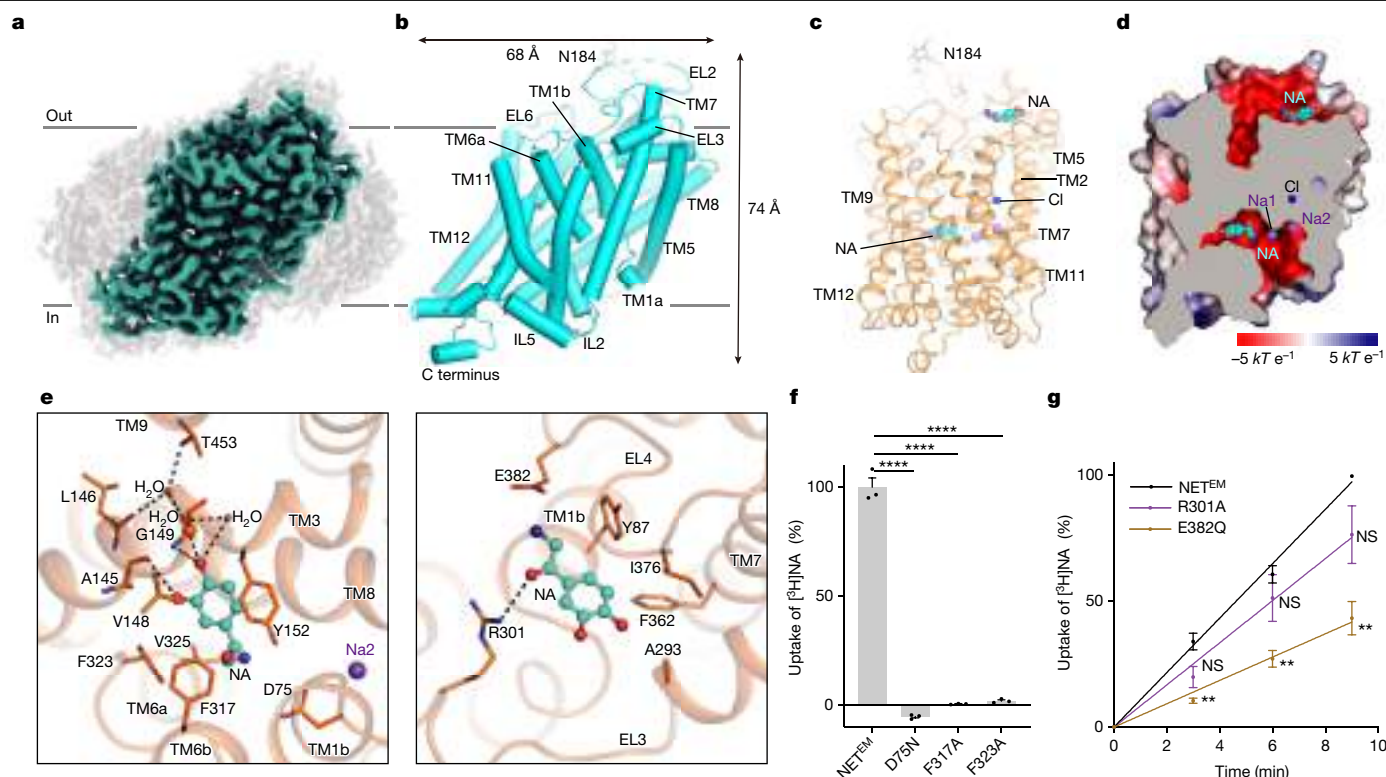
Fig. 1 | Cryo-EM structure of apo and noradrenaline-bound NET in the inward-open conformation. a, Cryo-EM map of apo NET (cyan) embedded in nanodisc (grey), captured in the inward-open conformation. **b**, Structure of the apo NET model. The dimensions of the model, transmembrane helices and loops are indicated. Glycosylation and disulfide bonds on the EL2 loop are shown as sticks. **c**, Molecular structure and binding position of noradrenaline. Noradrenaline molecules are shown as spheres, with their carbon backbone in cyan, and oxygen and nitrogen atoms in red and blue, respectively. Sodium and chloride ions are represented as purple and green spheres. **d**, Electrostatic surface cutaway depicting the binding mode of noradrenaline and Na$^+$ and Cl$^-$ ions to NET. **e**, The extensive interaction network within NET and noradrenaline in S1 and S2. Residues involved in interactions are shown as sticks. Hydrogen bonds interactions among noradrenaline, sodium ions, water molecules and NET are depicted as dashed lines. **f**, Comparative evaluation of the [^{3}H]noradrenaline ([^{3}H]NA) transportation activity of NET mutants in relation to the NET^{EM}. Data are mean ± s.e.m. from three independent assays, each with one measurement (n = 3). The transportation rate of D75N, F317A and F323A are significantly lower than that of wild-type NET^{EM}. $P < 0.0001$ for all mutants, unpaired t-test. **g**, Normalized initial transportation rates of [^{3}H]noradrenaline uptake into HEK293F expressing NET^{EM} and mutants in relation to the NET^{EM}. Data are mean ± s.e.m. from three independent experiments, each with a single measurement (n = 3). The initial transportation rate of E382Q ($P = 0.0008$) was significantly lower than that of wild-type NET^{EM}, whereas R301A ($P = 0.1335$) was not significantly different. Unpaired t-test. **$P < 0.01$, ****$P < 0.0001$; NS, not significant.

essential information for a full understanding of the physiological and pharmacological roles of NET.

Functional analysis and structure of NET

To gain insights into the molecular mechanisms governing transport and modulation of NET, we prepared a sample of full-length wild-type NET (NET^{WT}). Detergent-solubilized NET^{WT} was prone to severe aggregation, as evident from the size-exclusion chromatography (SEC) profile (Extended Data Fig. 1a). To improve its biochemical properties, we removed the first 51 unstructured N-terminal residues, resulting in the variant NET^{EM}, which had a sharper and more symmetrical SEC profile (Extended Data Fig. 1b). NET^{EM} had a similar Michaelis constant (K_m) for noradrenaline and similar half-maximal inhibition constants (IC$_{50}$) for χ-MrlA^{EM}, bupropion and ziprasidone relative to NET^{WT}, suggesting that the N-terminal truncation does not have a significant effect on the interactions with noradrenaline or these inhibitors (Extended Data Fig. 1c). We reconstituted purified NET^{EM} into nanodiscs using brain polar lipids and the scaffold protein MSP1D1E3 (Extended Data Fig. 1d,e). To ensure that NET^{EM} retained its transport function after purification, we reconstituted the protein into proteoliposomes with the same lipid composition used for the nanodisc preparation. The purified NET was able to transport [^{3}H]noradrenaline with a similar

K_m comparable to transport in HEK293 cells. Additionally, the drugs mentioned above showed similar potency in inhibiting NET transport activities in proteoliposomes and cells (Extended Data Fig. 1i–f and Extended Data Table 1). These findings confirm that NET is functional within the proteoliposome, suggesting that the nanodisc sample of NET reconstituted with brain polar lipids is active and able to assume all relevant conformational states for transport. Moreover, the inhibition constant (K_i) values for χ-MrlA^{EM}, bupropion and ziprasidone for NET in nanodiscs, determined using scintillation proximity assay with competition from [^{3}H]nisoxetine, were 144.3 ± 11.3 nM, 13.1 ± 1.4 μM and 163.7 ± 20.3 nM, respectively (Extended Data Fig. 1m–p). This suggests that the nanodisc sample effectively retains the ability to bind the investigated drugs after the purification and reconstitution process. We subsequently determined the structures of NET^{EM} in the apo state (with NaCl alone) and in the presence of noradrenaline, an analogue of χ-MrlA, bupropion or ziprasidone, at resolutions of 2.6 Å, 2.6 Å, 2.8 Å, 3.2 Å and 2.8 Å, respectively (Fig. 1a, Extended Data Fig. 2, Supplementary Figs. 2–5 and Extended Data Table 2).

In the apo state (NET^{Apo}) the structure measures 74 Å in height and 68 Å in diameter, and features a classical LeuT fold (Fig. 1b). transmembrane helix 1 (TM1) and TM6 contain a break at a position approximately halfway across the membrane bilayer. This nonhelical region, together with adjacent residues in TM3 and TM8, constitutes the binding pocket

Article

for substrates and ions[14,18,31,32]. The extracellular surface of NET is primarily composed of extracellular loop 2 (EL2) (F167–P233), EL4 (S363–T402) and EL6 (N539–P550). N-glycosylation of EL2 has been established as important for stability, surface trafficking and transport activity of NET[33]. In our structure, we observed one N-glycosylation at position N184 (Fig. 1b). The other potential glycosylation sites are unresolved in the structure, probably owing to their high mobility (Fig. 1b). Previous studies have demonstrated that NET possesses two alternatively spliced C-terminal exons, with the C-terminal region being crucial in regulating cell surface expression, stability and transport activity[34,35]. In our structure, the C-terminal region, comprising residues S583–I617, is clearly resolved (Extended Data Fig. 3), which offers a structural template for further investigation of the functional roles of this region.

Substrate recognition by NET

We determined the structure of the noradrenaline-bound NET complex (NET^{NA}) at a resolution of 2.6 Å and trapped in an inward-facing conformational state (Fig. 1c,d and Supplementary Fig. 2). The well-resolved cryo-EM map enabled us to identify a density in the central binding pocket as a noradrenaline molecule (Extended Data Fig. 4a). However, at a lower threshold level, we observed additional density extending toward the cytosol (Extended Data Fig. 4a). We speculate that there may be a small population of particles with noradrenaline bound at an alternative position, dissociating from NET. This observation is consistent with the notion that the substrate undergoes dissociation from the transporter in its inward-facing conformation. Further, we identified an additional noradrenaline molecule within the juxtamembrane region on the extracellular side (Extended Data Fig. 4b), although the corresponding cryo-EM density is slightly less pronounced than that in the central binding pocket. No discernible density was observed in either central binding pocket or in the same juxtamembrane region (Extended Data Fig. 4c,d) in the apo structure, suggesting the presence of noradrenaline in both locations. We termed these two substrate-binding sites S1 and S2, respectively. In the S1 site, the positively charged amine group of noradrenaline is coordinated by electrostatic interaction with the conserved acidic residue D75 in TM1 (D75^{TM1}), which is highly conserved among monoamine neurotransmitter transporters (Extended Data Fig. 5). The catechol ring of noradrenaline inserts into the space located between TM3 and TM8, establishing hydrogen bonds between catechol hydroxyls of noradrenaline and the carbonyl oxygen of A145^{TM3} (Fig. 1e). Three water molecules have been identified surrounding the hydroxyl group of the catechol ring. These water molecules have a role in establishing a hydrogen-bond network that bridges interactions between the hydroxyl groups of noradrenaline and the carbonyl oxygen of L146^{TM3}, as well as the hydroxyl oxygen of T453^{TM9} (Fig. 1e). Two phenylalanines, F317^{TM6} and F323^{TM6}, form a hydrophobic pocket, further accommodating the binding of substrate. A structural comparison of NET^{NA} and NET^{Apo} demonstrates a remarkable similarity in the conformation of residues proximal to the S1 site (Extended Data Fig. 4e,f). Mutations of the residues surrounding S1 site, including D75N, F317A and F323A, completely inhibit the transport capacity of NET (Fig. 1f).

The S2 site is formed by residues derived from Y87^{TM1b}, R301^{EL3}, F362^{TM7}, I376^{EL4} and E382^{EL4}. In particular, the positively charged amine group of noradrenaline establishes a salt bridge with E382^{EL4}, and the hydroxyl group of noradrenaline forms a hydrogen bond with the R301 (Fig. 1e). The presence of Y87^{TM1b}, A293^{EL3}, F362^{TM7} and I376^{EL4} in close proximity to the catechol ring further aid in binding to noradrenaline. Structural comparison between NET^{NA} and NET^{Apo} reveals that the conformation of residues surrounding the S2 site are nearly identical (Extended Data Fig. 4g). These residues engaged in noradrenaline binding within the S2 site are highly conserved across diverse species (Extended Data Fig. 4h). The E382Q mutation results in a reduced transport rate (Fig. 1g), suggesting that noradrenaline binding at this position is important for its functional role. However, the R301A

mutation does not have a significant effect on transport. Consequently, we cannot rule out the possibility that E382 is involved in interactions with other residues in a different conformation. Mutations of such residues might disrupt these interactions and consequently affect the transport activity of NET. Further studies are needed to determine the potential functional role of this binding site. The allosteric binding site for serotonin in SERT has been identified[36]. The S2 site of SERT is located slightly above the central binding cavity (Extended Data Fig. 4i). SERT E494 forms a salt bridge with the amine group of serotonin, and the indole group of serotonin is stabilized by T-shaped π–π stacking with F556. These two critical residues are replaced by T474 and S536 in NET, respectively, thus eliminating the ability of NET to bind a second substrate molecule in this site (Extended Data Fig. 4i). Conversely, the potential S2 site of NET is not conserved in SERT; the A293 residue in NET is substituted by F311 in SERT. The large side chain of SERT F311 introduces prominent steric hindrance with noradrenaline, preventing its association.

Allosteric inhibition by χ-MrIA

χ-MrIA has been identified as a potent, highly specific and non-competitive inhibitor of NET[22,23], with an IC$_{50}$ of approximately 1.26 μM. To understand how this peptide inhibitor interacts with and inhibits NET, we used χ-MrIA^{EM}, an analogue of χ-MrIA that exhibits a 30- to 40-fold higher potency[37] (Extended Data Figs. 6a–c). Notably, most residues of χ-MrIA^{EM} are conserved compared with χ-MrIA, albeit with some modifications (Fig. 2a). The IC$_{50}$ value of χ-MrIA^{EM} for inhibiting NET is 139.5 nM, around 10 times more potent than χ-MrIA and XEN2174 (Fig. 2b). We resolved the structure of NET bound to χ-MrIA^{EM} (NET^{MrIA}) at a resolution of 2.8 Å (Supplementary Fig. 3).

The cryo-EM map of NET^{MrIA} revealed an additional hairpin-shaped density representing the bound χ-MrIA^{EM} (Fig. 2c). The χ-MrIA^{EM} model includes two pairs of disulfide bonds and we further compared it with the NMR structure of χ-MrIA[38] (Extended Data Fig. 6d). Despite the backbones appearing almost identical, the side chains exhibit significant conformational changes. NET^{MrIA} is stabilized in an outward-facing conformational state (Fig. 2d,e). χ-MrIA^{EM} is positioned at the mouth of the cavity and extends into it, forming an angle of around 70° relative to the membrane plane, effectively blocking substrate access to the central binding cavity (Fig. 2d). χ-MrIA^{EM} features two positively charged residues, K9 and R12. K9 is located at the tip of the hairpin and projects into the cavity of NET, forming a salt bridge with D75^{TM1} (Fig. 2f,g). The side chain of K9 aligns parallel to that of O-methyl-L-tyrosine 8 (MeY8), and both side chains line up with the antiparallel β-strands of χ-MrIA^{EM}, further extending the beta sheet towards to bottom of the cavity. The iminazole group of R12 establishes multiple hydrogen bonds with K541^{EL6} and T544^{EL6} (Fig. 2h). MeY8 establishes extensive hydrophobic interactions with surrounding residues, including F71^{TM1a}, V148^{TM3}, F317^{TM6a}, F323^{TM6b} and A476^{TM10} (Fig. 2f,g). L10 nestles within a hydrophobic pocket formed by the side chains of W80^{TM1b}, I155^{TM3}, W158^{TM3}, A384^{EL4} and L469^{TM10} (Fig. 2g). Mutations at MeY8, K9 and L10 entirely abolish the inhibitory effects, underscoring the critical role of these residues in inhibition activity of the χ-MrIA[39]. Additionally, we identify several hydrogen bonds as crucial for the binding of χ-MrIA^{EM} to NET. For example, R81^{TM1b} and D473^{TM10} interact with χ-MrIA^{EM} through hydrogen bonds involving the backbone (Fig. 2h).

Structural comparison of NET^{MrIA} and NET^{NA} shows that the binding pockets for χ-MrIA and noradrenaline do not overlap, supporting the notion that χ-MrIA functions as a non-competitive inhibitor (Extended Data Figs. 6e,f). Structural comparison of NET^{MrIA} and nisoxetine-bound *Drosophila* DAT reveals a clear overlap in their binding pockets, consistent with the fact that the nisoxetine competitively inhibits binding of χ-MrIA to NET[23] (Extended Data Figs. 6g,h). χ-MrIA exhibits remarkable specificity in inhibiting NET activity and little effect on DAT or SERT[39]. Sequence alignments demonstrate that the position equivalent to L469
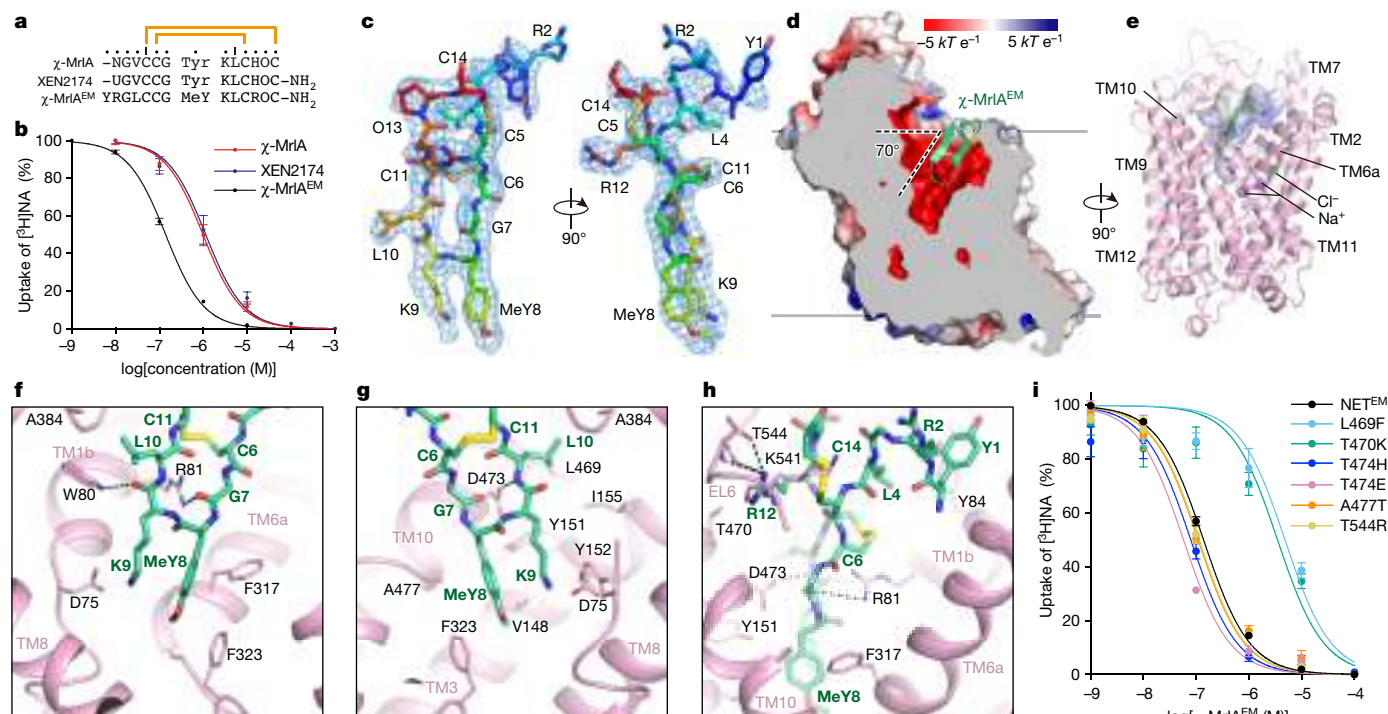
Fig. 2 | Allosteric binding site of χ-MrlA^EM in NET. a, Sequence alignment of χ-MrlA, XEN2174 and χ-MrlA^EM. Disulfide bonds between cysteine residues are depicted by orange lines. **b**, Inhibition of NET by χ-MrlA, XEN2174 and χ-MrlA^EM. Data are normalized mean ± s.e.m. from 4 biologically independent assays, each with triplicate measurements ($n = 12$). The IC_{50} value of χ-MrlA and XEN2174 are significantly higher than that of χ-MrlA^EM, with P values of 0.0037 and 0.0194, respectively (one-tailed t-test). **c**, Electron density of χ-MrlA^EM is shown as mesh, and the structure of χ-MrlA^EM is shown as sticks in rainbow. **d**, Surface electrostatic potential map of χ-MrlA^EM-bound NET (NET^MrlA). Cross-sectional view illustrating χ-MrlA^EM (green) binding within the negatively charged pocket of NET. **e**, Cartoon depiction of overall structure of NET^MrlA with surface electrostatic potential map of χ-MrlA^EM. Sodium and chloride ions are represented as purple and green spheres. **f–h**, Detailed interactions between χ-MrlA^EM (lime green) and NET (pink), focusing on the bottom front (**f**), the back (**g**), and the upper part (**h**) of χ-MrlA^EM. Residues participating in interactions are shown as sticks. Hydrogen-bond interactions are depicted with dashed lines. **i**, Potency of inhibition by χ-MrlA^EM on wild-type and mutant NET^EM. Data are normalized mean ± s.e.m. of each construct obtained from three biologically independent assays. Each sample was measured in triplicate ($n = 9$). Unpaired t-test performed for IC_{50} values indicated no significant differences from wild-type NET^EM for T544R ($P = 0.4149$), and significant differences for L469F ($P = 0.0008$), T470K ($P = 0.0002$), T474E ($P < 0.0001$), T474H ($P = 0.0011$) and A477T ($P = 0.0192$).

and T470 in NET are replaced by F472 and T473 in DAT and V489 and K470 in SERT, respectively (Extended Data Fig. 5). We carried out [³H] noradrenaline uptake assays on L469F, T470K, T474E, T474H, A477T and T544R mutants of NET^EM to assess the effects of these mutations on the inhibitory action of χ-MrlA^EM. χ-MrlA^EM inhibited NET^EM T474E, T474H, A477T and T544R mutants with IC_{50} values similar to that of the unmutated NET^EM. L469F and T470K mutations reduced the sensitivity of NET^EM to χ-MrlA^EM by approximately 30-fold (Fig. 2i). These results highlight the pivotal roles of F472 in DAT and K470 in SERT, which could be responsible for χ-MrlA discriminating between NET and the other monoamine transporters, DAT and SERT.

Conformational transitions of NET

The scaffold domain of NET^NA and NET^MrlA in different states aligns very well, while the remaining transmembrane helices and loops exhibit significant displacements (Fig. 3a). Comparing the outward-facing to inward-facing states, the extracellular ends of TM1b and TM6a of NET^NA are tilted by 30° and 20°, respectively, towards the scaffold domain. Consequently, these helices obstruct the extracellular pathway to the central binding pocket. By contrast, TM1a of NET^NA is tilted away from the scaffold domain by 45° relative to NET^MrlA, opening an intracellular cavity that allows substrate release (Fig. 3a). TM6b aligns well between NET^NA and NET^MrlA (Fig. 3a). Further inspection reveals that the intracellular half of TM1, including the unwound segment and TM1a, undergoes a 180° rotation between these two states (Fig. 3b). Comparing

these two structures, it is apparent that χ-MrlA^EM clashes with TM1b in the inward conformation, thus preventing conformational transition (Fig. 3b). The inward-facing NET^NA complex is further compared with the outward-facing DAT bound with noradrenaline[16]. The displacement of transmembrane helices involved in conformational transition is similar to those observed in above structural comparison between NET^NA and NET^MrlA. Owing to rearrangements of transmembrane helices, we found that the residues involving in coordinating substrate noradrenaline also undergo displacement and local conformational change of side chains. Specifically, compared to F319^TM6 in DAT, the side chain of F317^TM6 in NET is displaced towards the side chain of Y152^TM3, positioned directly above the noradrenaline (Extended Data Fig. 7a). D75^TM1 in NET (equivalent to D46^TM1 in DAT) is displaced towards the intracellular side owing to the lifting of TM1a on the intracellular side (Extended Data Fig. 7a). The local conformational changes result in an approximately 4.2 Å movement of amino group of noradrenaline. Moreover, the Cα–Cα distance between F323 in NET and F325 in DAT is approximately 2.0 Å and their benzyl rings form an angle of approximately 110°, pushing the catechol group of noradrenaline towards TM8, resulting in movement of approximately 2.3 Å of the centre of the benzene ring (Extended Data Fig. 7a). These observations suggest that during the transition from the outward-facing state to the inward-facing state, in addition to the major conformational change of TM1 and TM6 helices, the substrate and surrounding side chains also experience local conformational changes to facilitate binding of substrate to transporter. In addition to significant tilting of transmembrane helices, EL1 moves towards
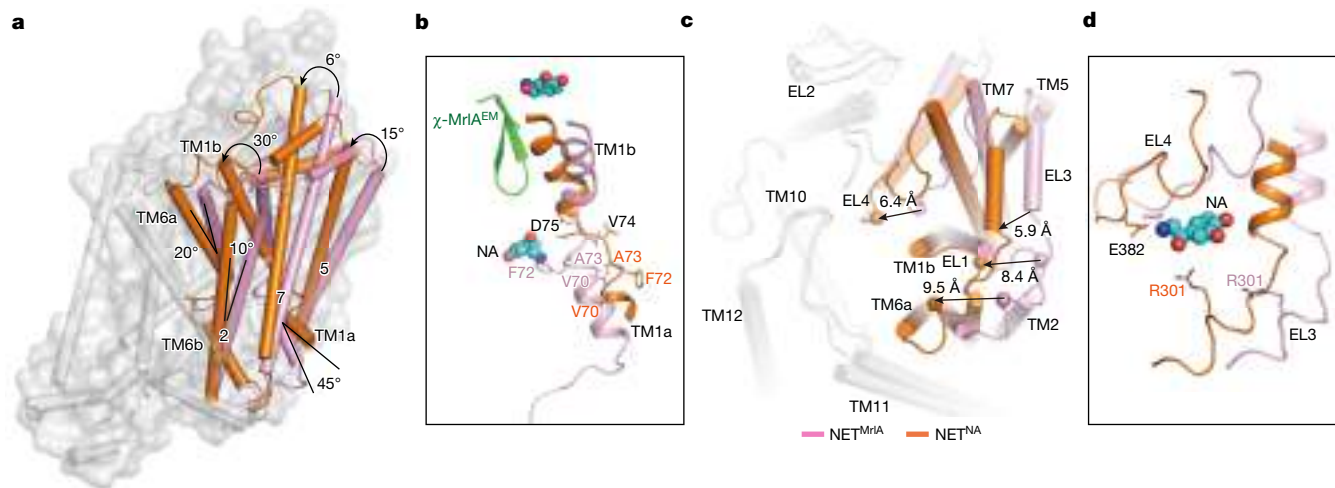
Fig. 3 | Conformational transition across functional states. a, Superposition of NET[MrlA] and NET[NA] aligned by the scaffold domain. Transmembrane helices and loops that exhibited significant conformational changes are shown in pink (NET[MrlA]) and orange (NET[NA]), respectively. The measured tilt angles of key transmembrane helices are indicated. b, Detailed conformational changes of TM1. MrlA[EM] is displayed as a green cartoon, and noradrenaline molecules are presented as orange spheres. Residues that undergo significant

conformational changes are displayed as sticks. c, Top view of the superposition of NET[MrlA] and NET[NA] aligned by the scaffold domain. The displacements of loops EL1, EL3 and EL4, measured using the Cα atoms of G92, R301 and E382 are indicated. d, Emphasis on the specific conformational shifts at the S2 site between NET[NA] and NET[MrlA]. Key residues involved in interactions with noradrenaline are depicted in stick form.

the scaffold domain by 8.4 Å (Cα–Cα distance of G92) to accommodate the conformational change in TM1 and TM2, and EL3 and EL4, sitting above EL1, are displaced towards the scaffold domain by 6.4 Å (Cα–Cα distance of E382) and 9.5 Å (for R301) (Fig. 3c), respectively. These significant rearrangements in both transmembrane helices and extracellular loops collectively lead to the formation of the S2 binding site of noradrenaline in the inward-facing conformation.

Sodium (Na^+) and chloride (Cl^-) ions have pivotal roles in facilitating ligand binding and transport within NET[4]. Our high-quality cryo-EM maps enabled us to identify the binding sites of these ions. In the outward-facing NET[MrlA] structure, Na1 is coordinated by the carbonyl oxygen of A73[TM1], S318[TM6a], the side-chain carbonyl oxygen of N78[TM1b], N350[TM7] and S318[TM6a], whereas the Na2 site is coordinated by the main-chain carbonyls of G71[TM1], V74[TM1] and L415[TM8], and the side-chain oxygens of S418[TM8] and D419[TM8] (Extended Data Fig. 6i). A chloride ion is positioned approximately 6.1 Å from the Na1 site, coordinated by the side-chain hydroxyls of Y98[TM6a], S318[TM6a] and S354[TM7], as well as the side-chain amides of N78[TM1] and Q314[TM6] (Extended Data Fig. 6i). In the noradrenaline-bound inward-facing structure, TM1a is markedly displaced, and tilts away from the scaffold domain compared with its position in the outward-facing state. The residues on TM1a, which are involved in coordinating sodium ions, shift away from the these ions, leading to a reduced coordination numbers of Na1 and Na2 (Extended Data Fig. 6j). Previous studies have shown that, similar to SERT, the ion-coupling stoichiometry between Na^+ and substrate in NET is 1:1 (refs. 40,41). Na1 has a crucial role in substrate binding in SERT, and the dissociation of Na2 from the transporter is coupled with a conformational transition of the transporter to an inward-facing state[42,43]. Given the conserved ion-binding pocket and sodium-coupling stoichiometry between NET and SERT, we speculate that the Na2 may have a similar role in NET, dissociating from the transporter in the cytosol and coupling Na^+ gradient to substrate transport. In the inward-facing NET[NA] complex, we placed a sodium ion in the Na2 binding pocket according to the cryo-EM map. However, only three bonds contribute to its binding, with bond lengths greater than 3 Å. Consequently, we cannot rule out the possibility this site may be occupied by a water molecule. Nonetheless, both scenarios suggest that Na2 cannot stably associate with the transporter in the inward-facing conformation, supporting the putative functional role of Na2.

Inhibition of NET function by bupropion

The α-aminophenone compound bupropion (Fig. 4a) selectively inhibits NET and DAT, with IC_{50} values of 5 μM and 2 μM, respectively[44], but has no inhibitory effect on SERT[45]. To explore the binding site of bupropion, we resolved the structure of bupropion-bound NET (NET[BPP]) at 2.8 Å (Fig. 4b and Supplementary Fig. 4). Similar to the NET[NA] complex, in the NET[BPP] complex structure, TM1a bends towards the membrane plane (Fig. 4c), indicating that the NET[BPP] complex also adopts an inward-open conformation. The aromatic meta-chloro substituent of bupropion extends to the interior of the binding cavity, whereas the tert-butyl amine group is oriented toward the cytosolic side (Fig. 4c,d). This tert-butyl amine group engages extensive hydrophobic interactions with A145[TM3], V148[TM3], Y152[TM3], F323[TM6] and F317[TM6]. D75[TM6] participates in stabilizing bupropion by forming hydrogen bonds with its acyl group (Fig. 4d). The tert-butyl amine group slots into the space between TM6 and TM8, and is cradled by residues G320[TM6], G422[TM8] and V325[TM6] (Fig. 4d). Mutation of V325 to a larger leucine, narrowing the space accommodate the tert-butyl amine group, yield a tenfold increase in the IC_{50} (Fig. 4e). When comparing the binding mode of noradrenaline to NET, the tert-butyl amine group of bupropion extends further towards the intracellular pathway (Fig. 4f). A structural comparison between NET[BPP] and NET[MrlA] structures reveals clear steric clashes between the tert-butyl amine group and F72 in the outward-open conformation (Fig. 4g). This observation suggests that the effect of bupropion binding is to obstruct the conformational transition of NET from an inward-facing to an outward-facing orientation. It also underscores the significance of the tert-butyl amine group in mediating the inhibitory action of bupropion, supported by the fact that analogues of bupropion with smaller amine substituents, such as N-methyl and primary amine, can act as transporter substrates[45].

To understand the molecular basis underlying the insensitivity of SERT to bupropion, we compared the structure of NET[BPP] with the serotonin-bound SERT in the inward-facing conformation. The overall structures are largely superimposable (Fig. 4h). However, residues within the central binding site are not strictly conserved. Residues V148, G149, S420 and G422 in NET are substituted by I172, A173, T439 and A411 in SERT. There is no obvious clash between bupropion and residues I172, A173 and T439 of SERT (Fig. 4h). By contrast, the alanine substitution in
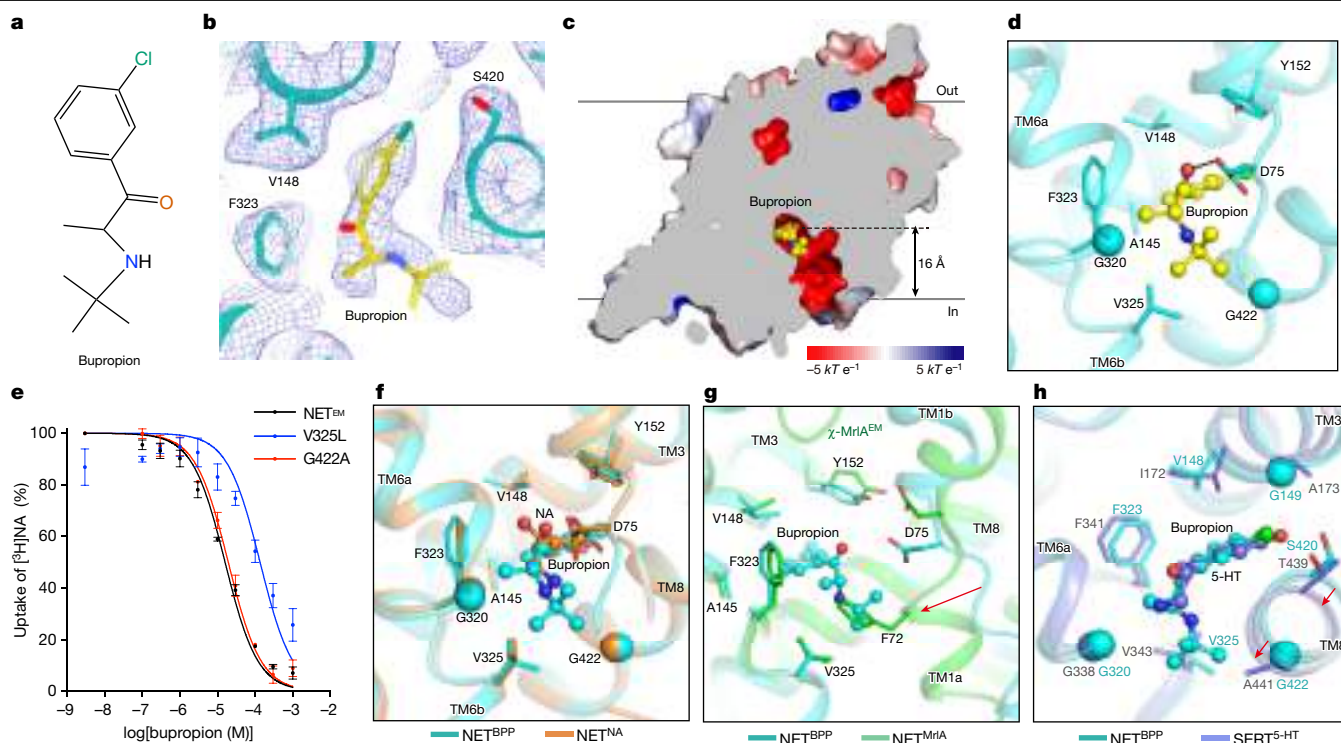
Fig. 4 | Mechanism of NET inhibition by bupropion. a, Molecular formula of bupropion. **b**, The electron densities of bupropion and surrounding residues are shown as mesh and the structure is visualized as sticks. Colours highlight oxygen, nitrogen and chloride atoms in red, blue and green, respectively. **c**, Cross-sectional view of the electrostatic surface of NET[BPP]. Bupropion is represented as yellow spheres. The distance between the head of bupropion and the intracellular membrane is indicated. **d**, Interaction network between bupropion and NET. Key residues involved in the interaction are shown as sticks. **e**, Inhibition of noradrenaline transport by bupropion in wild-type and mutant NET[EM]. Data are normalized mean ± s.e.m. of each construct from 3 biologically independent assays, each with a single measurement ($n = 3$).

Curves were generated by non-regression analysis. Unpaired t-test comparing IC$_{50}$ of wild-type versus mutant NET[EM]. IC$_{50}$ of NET[EM](G422A) ($P = 0.5476$) was not significantly different, whereas IC$_{50}$ of NET[EM](V325L) ($P = 0.0011$) was significantly higher than for wild-type NET[EM]. **f**, Structural superposition of NET[EM] and NET[BPP] aligned by scaffold domain. NET[BPP] is depicted in cyan and NET[NA] is in orange. **g**, Superposition between NET[MrIA] (green) and NET[BPP] (cyan) based on the scaffold domain. F72 of NET[MrIA] has a spatial clash with bupropion. **h**, Superposition between the serotonin-binding site of SERT (SERT[5-HT]) (Protein Data Bank (PDB): 7LI9) (slate) and NET[BPP] (cyan) based on overall structure.

SERT, at the equivalent position of G422[TM8] in NET, near the *tert*-butyl amine group, potentially generates steric hindrances with bupropion (Fig. 4h). This observation is in line with a previous study showing that the volume of the *tert*-butyl amine group is vital for the selectivity of bupropion[45]. However, the G422A mutant exhibits a similar IC$_{50}$ value (19.4 µM) to that of NET[EM] (14.8 µM) (Fig. 4e). We speculate that additional structural discrepancies may also contribute to the resistance of SERT to bupropion. Further structural inspection reveals that TM6a on one side of the *tert*-butyl amine group aligns well, whereas TM8 on the opposite side is significantly displaced (Fig. 4h). This displacement reduces the space between TM6a and TM8, aggravating steric interference between A411 and bupropion in SERT compared with the NET G422A mutant. Such a local displacement of TM8 between NET and SERT in their inward-facing conformations is postulated to arise from amino acid variations across a broad spatial area, which might create a distinct interaction network, thereby stabilizing the TM8 helix in a different orientation.

Recognition of the ziprasidone-binding site

Ziprasidone serves as an adjunctive therapy for major depressive disorder due to its capability to inhibit the neuronal uptake of noradrenaline and serotonin[46]. To investigate the molecular mechanism by which ziprasidone inhibits NET, we determined the complex structure of NET with ziprasidone at a resolution of 3.2 Å (Supplementary Fig. 5). A cane-shaped density was observed on the inner leaflet of the

membrane plane, which agrees well with the shape of the ziprasidone molecule (Fig. 5a,b). Ziprasidone binding is accommodated within a cavity formed by TM2, TM6b, TM7 and TM8, which opens towards the intracellular side, consistent with the NET[ZPD] complex adopting an inward-facing conformational state (Fig. 5c). The 1,2-benzisothiazolin group of ziprasidone aligns approximately parallel to the membrane plane and extends to the base of the cavity, establishing extensive hydrophobic interactions with A145[TM3], V148[TM3], Y152[TM3] and F323[TM6] (Fig. 5d). The 1-ethylpiperazine group, which bridges the 1,2-benzisothiazolin and 6-chloroindolin-2-one groups, forms a hydrogen bond with D75[TM1] (Fig. 5d). The chlorindolin group is situated at the entrance of the cavity, interacting with F72[TM1], V325[TM6b], L326[TM6b] and F329[TM6b]. Mutation of V325 to a larger leucine residue result in a nearly sixfold increase in IC$_{50}$ (Fig. 5e), probably owing to steric clashes with ziprasidone. The complex structures of NET[ZPD] and NET[NA] are nearly identical (Fig. 5f). However, both the backbone and side chains of the unwound segment between TM1a and TM1b are significantly different in the ziprasidone structure. Specifically, this segment in NET[NA] structure is straighter than that in the NET[ZPD] complex. Moreover, whereas the side chain of F72 faces outward in the NET[NA] structure, it is rotated by 180° in the NET[ZPD] complex, and engages in interactions with ziprasidone (Fig. 5f).

A previous report indicated that ziprasidone inhibits all three types of monoamine transporters[47]. To understand the structural basis for the distinct selectivity of ziprasidone compared with bupropion, we superimposed the NET[ZPD] structure onto the serotonin-bound inward-open structure of SERT. As previously discussed, the bulky *tert*-butyl amine
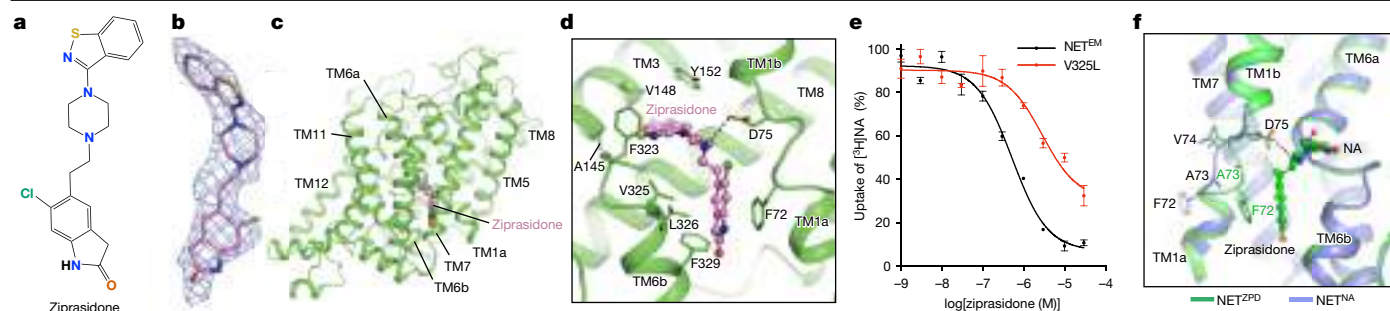
Fig. 5 | Antagonism of NET by ziprasidone. a, Molecular formula of ziprasidone. **b**, Electron density map of ziprasidone. **c**, Cartoon depiction of the model of the NET–ziprasidone complex. Ziprasidone is depicted in pink spheres. **d**, Magnified view of the interaction network between NET and ziprasidone. Residues involved in the interaction are shown as sticks. **e**, Inhibition potency of ziprasidone on wild-type and mutant NET^{EM}. Data are normalized mean ± s.e.m. for each construct from 3 biologically independent assays, each with single measurement ($n = 3$). Curves were generated by non-regression analysis, yielding IC_{50} values of 525.0 ± 9.2 nM for NET^{EM} and 2.9 ± 0.57 µM for NET^{EM}(V325L). Unpaired t-test on the IC_{50} values revealed that the IC_{50} value of V325L was significantly higher than NET^{EM} ($P = 0.009$). **f**, Comparison of the local conformation of NET surrounding ziprasidone. Superposition between NET^{ZPD} (green) and NET^{NA} (slate) based on the scaffold domain.

group of bupropion is positioned between G320 and G422, probably creating a significant steric hindrance with A441 of SERT (Extended Data Fig. 7b,c). This location is occupied by a more streamlined ethane group in ziprasidone, which acts as a linker between the 6-chloroindolin-2-one and piperazine groups (Extended Data Fig. 7d). This is more compatible with the narrower space between $G338^{TM6}$ and $A411^{TM8}$ in SERT. We further compared the binding site of bupropion and ziprasidone with that of ibogaine in SERT, observing that ibogaine occupies the space between TM3 and TM8, leading to a significant displacement of TM8 compared with the positions in the NET structures bound to either bupropion or ziprasidone (Extended Data Fig. 7e). Such structural insights highlight the differences in how these drugs inhibit these transporters.

Discussion

Here we determined an ensemble of structures of human NET in NaCl, in the apo state and in complex with the substrate noradrenaline, an analogue of χ-MrlA, bupropion and ziprasidone (Extended Data Fig. 8). These structures are captured in two fundamental functional states: the outward-facing and inward-facing conformations. Bound sodium and chloride ions are observed in both conformations, shedding light on the coordination changes as NET transitions between its functional states. The structure of noradrenaline-bound NET provides insights on the detailed binding of noradrenaline at the central orthosteric site. In the presence of NaCl, structures of SERT in both its apo or substrate-bound states have been resolved in outward-facing, occluded and inward-facing states[36], and structures of DAT have been determined in their outward-facing state[15,16]. Here we elucidate structures of apo and noradrenaline-bound NET in the inward-facing states. The structures of DAT and NET exhibit different conformational preferences. We speculate that mutations used in structural studies of DAT, which enhance its thermostability[15], may also influence its conformational preference. Additionally, previous studies have shown that cholesterol has a crucial role in maintaining the outward-facing conformation of DAT[15,48], and might similarly influence NET[49]. The DAT structure was determined with a high concentration of cholesteryl hemisuccinate, whereas we used brain polar lipids in the nanodisc reconstitution of NET. Given the non-polar nature of cholesterol, we speculate that the its content in brain polar lipid may not be sufficient to stabilize the transporter in its outward-facing state. Further research is needed to understand the functional role of cholesterol in regulating the conformational transition of NET.

The conotoxin χ-MrlA selectively and non-competitively inhibits the transport activity of NET, but has no such effect on SERT and DAT[23].

The structure of χ-$MrlA^{EM}$-bound NET reveals that the antiparallel β-sheet structure of χ-$MrlA^{EM}$ obstructs the extracellular pathway leading to the central binding pocket and stabilizes NET in its outward-facing conformational state. Bound χ-$MrlA^{EM}$ does not overlap with the noradrenaline-binding pocket. Our mutagenesis experiments indicate that the F472 in DAT and K490 in SERT are essential for rendering SERT and DAT resistant to χ-$MrlA^{EM}$ (Fig. 2i and Extended Data Fig. 5). G422, which is conserved in NET and DAT, is replaced by A441 in SERT. Because of local differences in TM8 of SERT, pronounced steric hindrances are observed between A441 and bupropion, suggesting a possible reason for SERT resistance to bupropion. Despite binding in the same inward-facing conformational state as bupropion, ziprasidone also acts as a potent inhibitor of SERT. Unlike bupropion, which has a bulky *tert*-butyl amine group situated in the space between TM6 and TM8, ziprasidone features a much narrower ethane group at the same position, which partly accounts for SERT being relatively more susceptible to inhibition by ziprasidone than bupropion. The binding pockets of bupropion and ziprasidone face the cytosol. This prompts the question of how these drugs access their respective binding sites. Given that the physicochemical properties of these two orally bioavailable drugs adhere to Lipinski's rule of five and Veber's rules, we suggest that both drugs are likely to possess good membrane permeability[50]. Bupropion has been reported to function as a pharmacological chaperone, rescuing disease-causing, misfolded DATs or NET accumulation in the endoplasmic reticulum[30]. These findings suggest that bupropion and ziprasidone can penetrate the membrane, and may initially bind the transporter on the cytosolic side. However, we cannot completely rule out the possibility that bupropion and ziprasidone may enter through the transporter, and remain bound in the inward-facing state, thereby inhibiting transport activity, as shown in a recent study in which tiagabine binds in this manner to GAT1[32]. These insights from our structural studies of NET provide a foundation for the further development of next-generation drugs targeting NET and other monoamine transporters.

Online content

Any methods, additional references, Nature Portfolio reporting summaries, source data, extended data, supplementary information, acknowledgements, peer review information; details of author contributions and competing interests; and statements of data and code availability are available at https://doi.org/10.1038/s41586-024-07638-z.

1. Silverberg, A. B., Shah, S. D., Haymond, M. W. & Cryer, P. E. Norepinephrine: hormone and neurotransmitter in man. *Am. J. Physiol.* **234**, E252 (1978).
2. Pacholczyk, T., Blakely, R. D. & Amara, S. G. Expression cloning of a cocaine-and antidepressant-sensitive human noradrenaline transporter. *Nature* **350**, 350–354 (1991).

3. Mandela, P. & Ordway, G. A. The norepinephrine transporter and its regulation. *J. Neurochem.* **97**, 310–333 (2006).
4. Kristensen, A. S. et al. SLC6 neurotransmitter transporters: structure, function, and regulation. *Pharmacol. Rev.* **63**, 585–640 (2011).
5. Brust, A. et al. χ-Conopeptide pharmacophore development: toward a novel class of norepinephrine transporter inhibitor (Xen2174) for pain. *J. Med. Chem.* **52**, 6991–7002 (2009).
6. Llorca-Torralba, M., Borges, G., Neto, F., Mico, J. A. & Berrocoso, E. Noradrenergic locus coeruleus pathways in pain modulation. *Neuroscience* **338**, 93–113 (2016).
7. Pertovaara, A. Noradrenergic pain modulation. *Prog. Neurobiol.* **80**, 53–83 (2006).
8. Berridge, C. W., Schmeichel, B. E. & España, R. A. Noradrenergic modulation of wakefulness/arousal. *Sleep Med. Rev.* **16**, 187–197 (2012).
9. Sapolsky, R. M., Romero, L. M. & Munck, A. U. How do glucocorticoids influence stress responses? Integrating permissive, suppressive, stimulatory, and preparative actions. *Endocr. Rev.* **21**, 55–89 (2000).
10. Jansen, A. S., Nguyen, X. V., Karpitskiy, V., Mettenleiter, T. C. & Loewy, A. D. Central command neurons of the sympathetic nervous system: basis of the fight-or-flight response. *Science* **270**, 644–646 (1995).
11. Bobb, A. J. et al. Support for association between ADHD and two candidate genes: NET1 and DRD1. *Am. J. Med. Genet. B* **134**, 67–72 (2005).
12. Lake, C. R. et al. High plasma norepinephrine levels in patients with major affective disorder. *Am. J. Psychiatry* **139**, 1315–1318 (1982).
13. Bohn, L. M., Xu, F., Gainetdinov, R. R. & Caron, M. G. Potentiated opioid analgesia in norepinephrine transporter knock-out mice. *J. Neurosci.* **20**, 9040–9045 (2000).
14. Penmatsa, A., Wang, K. H. & Gouaux, E. X-ray structure of dopamine transporter elucidates antidepressant mechanism. *Nature* **503**, 85–90 (2013).
15. Wang, K. H., Penmatsa, A. & Gouaux, E. Neurotransmitter and psychostimulant recognition by the dopamine transporter. *Nature* **521**, 322–327 (2015).
16. Pidathala, S., Mallela, A. K., Joseph, D. & Penmatsa, A. Structural basis of norepinephrine recognition and transport inhibition in neurotransmitter transporters. *Nat. Commun.* **12**, 2199 (2021).
17. Coleman, J. A. & Gouaux, E. Structural basis for recognition of diverse antidepressants by the human serotonin transporter. *Nat. Struct. Mol. Biol.* **25**, 170–175 (2018).
18. Coleman, J. A., Green, E. M. & Gouaux, E. X-ray structures and mechanism of the human serotonin transporter. *Nature* **532**, 334–339 (2016).
19. Coleman, J. A. et al. Serotonin transporter–ibogaine complexes illuminate mechanisms of inhibition and transport. *Nature* **569**, 141–145 (2019).
20. Plenge, P. et al. The antidepressant drug vilazodone is an allosteric inhibitor of the serotonin transporter. *Nat. Commun.* **12**, 5063 (2021).
21. Paczkowski, F. A., Sharpe, I. A., Dutertre, S. & Lewis, R. J. χ-Conotoxin and tricyclic antidepressant interactions at the norepinephrine transporter define a new transporter model. *J. Biol. Chem.* **282**, 17837–17844 (2007).
22. Sharpe, I. A. et al. Two new classes of conopeptides inhibit the α1-adrenoceptor and noradrenaline transporter. *Nat. Neurosci.* **4**, 902–907 (2001).
23. Sharpe, I. A. et al. Inhibition of the norepinephrine transporter by the venom peptide χ-MrIA: site of action, Na⁺ dependence, and structure–activity relationship. *J. Biol. Chem.* **278**, 40317–40323 (2003).
24. Zhang, Y. W., Turk, B. E. & Rudnick, G. Control of serotonin transporter phosphorylation by conformational state. *Proc. Natl Acad. Sci. USA* **113**, E2776–E2783 (2016).
25. Ramamoorthy, S., Shippenberg, T. S. & Jayanthi, L. D. Regulation of monoamine transporters: role of transporter phosphorylation. *Pharmacol. Ther.* **129**, 220–238 (2011).
26. Hillhouse, T. M. & Porter, J. H. A brief history of the development of antidepressant drugs: from monoamines to glutamate. *Exp. Clin. Psychopharmacol.* **23**, 1–21 (2015).
27. Hahn, M. K., Robertson, D. & Blakely, R. D. A mutation in the human norepinephrine transporter gene (*SLC6A2*) associated with orthostatic intolerance disrupts surface expression of mutant and wild-type transporters. *J. Neurosci.* **23**, 4470–4478 (2003).
28. Kurian, M. A. et al. Homozygous loss-of-function mutations in the gene encoding the dopamine transporter are associated with infantile parkinsonism-dystonia. *J. Clin. Invest.* **119**, 1595–1603 (2009).
29. Kurian, M. A. et al. Clinical and molecular characterisation of hereditary dopamine transporter deficiency syndrome: an observational cohort and experimental study. *Lancet Neurol.* **10**, 54–62 (2011).
30. Beerepoot, P., Lam, V. M. & Salahpour, A. Pharmacological chaperones of the dopamine transporter rescue dopamine transporter deficiency syndrome mutations in heterologous cells. *J. Biol. Chem.* **291**, 22053–22062 (2016).
31. Shahsavar, A. et al. Structural insights into the inhibition of glycine reuptake. *Nature* **591**, 677–681 (2021).
32. Motiwala, Z. et al. Structural basis of GABA reuptake inhibition. *Nature* **606**, 820–826 (2022).
33. Melikian, H. E., Ramamoorthy, S., Tate, C. G. & Blakely, R. D. Inability to N-glycosylate the human norepinephrine transporter reduces protein stability, surface trafficking, and transport activity but not ligand recognition. *Mol. Pharmacol.* **50**, 266–276 (1996).
34. Sogawa, C. et al. C-terminal region regulates the functional expression of human noradrenaline transporter splice variants. *Biochem. J.* **401**, 185–195 (2007).
35. Bauman, P. A. & Blakely, R. D. Determinants within the C-terminus of the human norepinephrine transporter dictate transporter trafficking, stability, and activity. *Arch. Biochem. Biophys.* **404**, 80–91 (2002).
36. Yang, D. & Gouaux, E. Illumination of serotonin transporter mechanism and role of the allosteric site. *Sci. Adv.* **7**, eabl3857 (2021).
37. Lewis, R. J., Alewood, P. F., Alewood, D. & Palant, E. Type II chi-conotoxin peptides (noradrenaline transporter inhibitors). US Patent US7507717B2 (2009).
38. Nilsson, K. P. R. et al. Solution structure of χ-conopeptide MrIA, a modulator of the human norepinephrine transporter. *Pept. Sci.* **80**, 815–823 (2005).
39. Sharpe, I. A. et al. Inhibition of the norepinephrine transporter by the venom peptide chi-MrIA. Site of action, Na+ dependence, and structure-activity relationship. *J. Biol. Chem.* **278**, 40317–40323 (2003).
40. Gu, H. H., Wall, S. & Rudnick, G. Ion coupling stoichiometry for the norepinephrine transporter in membrane vesicles from stably transfected cells. *J. Biol. Chem.* **271**, 6911–6916 (1996).
41. Ramamoorthy, S. et al. Expression of a cocaine-sensitive norepinephrine transporter in the human placental syncytiotrophoblast. *Biochemistry* **32**, 1346–1353 (1993).
42. Koldsø, H. et al. Unbiased simulations reveal the inward-facing conformation of the human serotonin transporter and Na(+) ion release. *PLoS Comput. Biol.* **7**, e1002246 (2011).
43. Felts, B. et al. The two Na⁺ sites in the human serotonin transporter play distinct roles in the ion coupling and electrogenicity of transport. *J. Biol. Chem.* **289**, 1825–1840 (2014).
44. Ascher, J. A. et al. Bupropion: a review of its mechanism of antidepressant activity. *J. Clin. Psychiatry* **56**, 395–401 (1995).
45. Shalabi, A. R., Walther, D., Baumann, M. H. & Glennon, R. A. Deconstructed analogues of bupropion reveal structural requirements for transporter inhibition versus substrate-induced neurotransmitter release. *ACS Chem. Neurosci.* **8**, 1397–1403 (2017).
46. Schmidt, A. W., Lebel, L. A., Howard, H. R. & Zorn, S. H. Ziprasidone: a novel antipsychotic agent with a unique human receptor binding profile. *Eur. J. Pharmacol.* **425**, 197–201 (2001).
47. Cross, A. J. et al. Quetiapine and its metabolite norquetiapine: translation from in vitro pharmacology to in vivo efficacy in rodent models. *Br. J. Pharmacol.* **173**, 155–166 (2016).
48. Hong, W. C. & Amara, S. G. Membrane cholesterol modulates the outward facing conformation of the dopamine transporter and alters cocaine binding. *J. Biol. Chem.* **285**, 32616–32626 (2010).
49. Zeppelin, T., Ladefoged, L. K., Sinning, S., Periole, X. & Schiøtt, B. A direct interaction of cholesterol with the dopamine transporter prevents its out-to-inward transition. *PLoS Comput. Biol.* **14**, e1005907 (2018).
50. Veber, D. F. et al. Molecular properties that influence the oral bioavailability of drug candidates. *J. Med. Chem.* **45**, 2615–2623 (2002).

Article

Methods

Protein expression and purification

The DNA fragment encoding human NET (UniProt ID: P23975) was amplified from a human cDNA library. The DNA fragment of NET (N-terminal 51-residues truncated), along with an N-terminal tag containing a Twin-Strep tag, a superfolder GFP (sfGFP) and an HRV-3C restriction site, was inserted into a modified pEG BacMam vector. This construct was subsequently expressed in HEK293F cells using the Bac-to-Bac baculovirus expression system (Invitrogen). In brief, P1 and P2 viruses were prepared using sf9 insect cells. The P2 viruses were utilized to infect HEK293F when the cell density reached 2.5×10^6 cells per ml, supplemented with 1% (v/v) fetal bovine serum. The cells was cultured at 37 °C with 5% CO_2 and agitated at 100 rpm in suspension. 12 h post-infection, sodium butyrate (10 mM) was introduced to enhance protein expression level. Cells were harvested 48 h later, flash-frozen using liquid nitrogen, and stored at −80 °C for further use.

All subsequent procedures were conducted at 4 °C or on ice unless otherwise specified. Cells expressing NET were resuspended and lysed in buffer A (20 mM HEPES, 150 mM NaCl, pH 7.5) supplemented with protease inhibitors (aprotinin (2 μg ml^{-1}), leupeptin (1.4 μg ml^{-1}), pepstatin A (0.5 μg ml^{-1}) (MedChemExpress)) using a Dounce homogenizer. Membranes were collected by centrifugation at 38,000 rpm for 1 h and then solubilized in buffer B (buffer A supplemented with 1% (w/v) n-dodecyl β-D-maltoside (DDM) and 0.15% (w/v) cholesteryl hemisuccinate). Insoluble debris was removed by centrifugation at 38,000 rpm for 30 min, and the supernatant was filtered through a 0.22-μm filter membrane. Subsequently, the supernatant was passed through Streptactin Beads (Smart-Lifesciences) preequilibrated with purification buffer C (buffer A supplemented with 0.025% DDM). The beads were washed with ten column volumes of wash buffer C to remove unbound protein. The NET protein was then eluted with elution buffer D (buffer A supplemented with 5 mM D-desthiobiotin (Sigma-Aldrich, USA)) and concentrated to 1 ml using a 50 kDa MWCO Amicon (Millipore). Subsequently, the concentrated sample was analysed by SEC using a Superose 6 Increase 10/300 GL gel filtration column (GE Healthcare). The peak fractions were concentrated for nanodisc reconstitution.

To prepared NET samples bound with substrate noradrenaline, χ-MrIA^{EM}, bupropion and ziprasidone, we resuspended the collected HEK293F cells expressing NET and incubated them with these ligands for 1 h at concentrations of 30 μM, 2 μM, 20 μM and 5 μM, respectively. These ligand concentrations were maintained throughout the purification process. To ensure that the ligand could bound effectively with NET sample, we increased the concentration of noradrenaline, χ-MrIA^{EM}, bupropion and ziprasidone to 500 μM, 300 μM, 500 μM and 250 μM, respectively, during nanodisc reconstitution. Furthermore, we added 10 mM, 2 mM, 4 mM and 250 μM of these ligands to the cryo-EM samples 30 min before freezing the samples for cryo-EM analysis.

Nanodisc reconstitution

Brain Polar Lipid Extract (Porcine) (Avanti Polar Lipids, 141101P) was solubilized with 40 mM DDM under gentle rotation at room temperature for 30 min. Freshly prepared NET protein, MSP1D1E3 and solubilized lipid were mixed at a molar ratio of 1: 5: 200 for 1 h at 4 °C on a rotating mixer. Bio-Beads SM-2 (400 mg ml^{-1}) were added to remove detergent at 0 h, 2 h, and 4 h and then incubated overnight. After the Bio-Beads were removed, the supernatant was passed through Streptactin Beads and washed with 5 column volumes of purification buffer (20 mM HEPES, 150 mM NaCl, pH 7.5) to remove empty nanodiscs. The protein was then eluted from resin using elution buffer (20 mM HEPES, 150 mM NaCl, pH 7.5, 5 mM D-desthiobiotin). The Twin-Strep tag and sfGFP were cleaved with HRV-3C protease for 1 h on ice. The cleavage fragments were eliminated by a Ni-NTA column. Subsequently, the cleaved protein was concentrated to 1 ml and analysed by SEC using a Superose 6 Increase 10/300 GL gel filtration column with a running buffer of 20 mM HEPES, 150 mM NaCl, pH 7.5. The peak fraction within 14.5–15.5 ml was pooled and concentrated to 5–10 mg ml^{-1} for cryo-EM sample preparation.

Peptide synthesis

The peptides were chemically synthesized using a solid-phase peptide synthesis (SPPS) strategy based on Fmoc chemistry as previously described[51]. Taking χ-MrIA^{EM} as an example, Rink amide resin was subjected to 1 h swelling and Fmoc deprotection process with a 20% piperidine solution. The coupling of amino acids was carried out employing N,N-dimethylformamide as the solvent with the addition of Fmoc-protected amino acids, O-(6-chlorobenzotriazol-1-yl)-N,N,N',N'-tetramethyluronium hexafluorophosphate and N,N-diisopropylethylamine at room temperature for 1 h, followed by the addition of 20% piperidine for 30 min to remove the Fmoc protection group. Subsequently, the coupling-deprotection cycle was reiterated until the assembly of the peptide chain was completed. For peptide χ-MrIA^{EM} regioselective oxidation, the two-steps orthogonal synthesis strategy was employed, in which Fmoc-Cys(Trt)-OH was used at positions Cys^I and Cys^{IV}, whereas Fmoc-Cys(Acm)-OH was introduced at positions Cys^{II} and Cys^{III}. The Roman numerals represents the order of the cystein residues from the N-terminus of the peptide. χ-MrIA^{EM} was cleaved from the resin using TFA cleavage solution (TFA:triisopropylsilane:H_2O 90:5:5) for 3 h. Air oxidation was utilized to form the first pair of disulfide bond, followed by iodine oxidation to create the second pair of disulfide bond. The semi-preparative reversed phase high performance liquid chromatography (RP-HPLC) was used for the purification of the crude peptide product, and then freeze-drying was performed to obtained final products. The final purity and molecular weight of peptide were evaluated through analytical RP-HPLC and mass spectrometry, respectively. The final purity of all peptides were more than 95%.

Cryo-EM sample preparation and data acquisition

The freshly prepared NET in nanodisc was concentrated to approximately 10 mg ml^{-1} using a 50 kDa MWCO Amicon filter. Grids (Quantifoil Cu R1.2/1.3 300 mesh) were discharged in the presence of H_2 and O_2 for 60 s. A 2.5 μl droplet of prepared sample was applied to the grid and then blotted for 4–6 s at 4 °C under condition of 100% humidity and then vitrified in liquid ethane using a Vitrobot Mark IV (Thermo Fisher Scientific).

Cryo-EM data were collected using EPU (Thermo Fisher Scientific) on a Titan Krios electron microscope (Thermo Fisher Scientific) equipped with a K3 direct electron detector (Gatan) and a BioContinuum Imaging Filter (Gatan; slit width 20 eV). The movies were collected with a nominal magnification of 105,000×, yielding a pixel size of 0.85 Å on images. The dose rate was set to ~20 e$^-$ pixel^{-1} s^{-1} with a defocus value ranging from −1.0 to −2.0 μm. Each movie stack was dose-fractioned into 32 frames and was recorded with a total dose of ~60 e$^-$ Å^{-2}. The statistics of cryo-EM data are summarized in Extended Data Table 2.

Data processing

For the dataset of NET^{Apo}, 1,202 movie stacks were collected. The beam-induced motion was corrected by MotionCor2[52], and contrast transfer function (CTF) parameters were estimated by patch CTF estimation[53]. Micrographs were used for particle picking in cryoSPARC[54]. A total of 741,983 particles were picked and subjected to three rounds of 2D classification to remove non-particle picks and apparent junk particles. For the last round of 2D classification, only classes featuring transmembrane helices were selected, resulting in 12 classes and a particle set of 134,604 particles. These particles were used for ab-initio reconstruction (initial alignment resolution of 12 Å, maximum resolution of 6 Å, initial minibatch size of 300, final minibatch size of 1,000) and generated a map with typical transmembrane helix densities. Furthermore, seed-facilitated 3D classification was used to obtain

more homogeneous particles from the 741,983 particles and the seed particle set is the 134,604 particles. The specific method is to divide the 741,983 particles evenly into 5 groups, about 148,000 particles in each group are combined with 134,604 particles to deduplicate and carry out heterogeneous refinement for 3D classification. Subsequently, all good classes in each heterogeneous refinement job were combined and deduplicated, and finally 268,436 particles are obtained. The 788,431 particles were subjected non-uniform refinement, which yielded a reconstruction to 2.9 Å resolution. To improve map resolution, local refinement was applied with a tight transmembrane domain mask, which generated a 2.6 Å map using the gold-standard Fourier shell correlation criterion.

A similar strategy was applied in the data processing of NET[NA], NET[MrlA], NET[BPP] and NET[ZPD]. Specifically, a total of 2,321,152, 2,014,262, 2,009,739 and 1,117,052 particles were picked from 3,315, 3,422, 2,871 and 3,288 micrographs, respectively. After performing seed-facilitated 3D classification, 361,801, 313,089, 584,926 and 375,649 particles remained, yielding 3D reconstructions at 2.8 Å, 2.8 Å, 2.8 Å and 3.2 Å resolution respectively, according to the GSFSC criterion.

Model building
De novo model building of NET[Apo] was initiated using the 2.6 Å map in COOT[55]. The cryo-EM map of NET[NA] showed clear densities for most side chains, which allowed us to reliably build and adjust the model. Model building of NET[NA], NET[MrlA], NET[BPP] and NET[ZPD] was started by fitting the NET[Apo] structure into corresponding maps. Manual adjustments were carried out aided by discernible backbone and side-chain features. The crystal structure of SERT has revealed the binding pockets for sodium and chloride ions[18]. Given that the ion-binding sites are conserved between NET and SERT (Extended Data Fig. 6), we have assigned the corresponding ions to the extra density observed within these binding sites. Two-dimensional structures of noradrenaline, bupropion and ziprasidone were downloaded from PubChem, followed by the generation of the ligand restraint files for refinement by PHENIX[56]. The final model of all the datasets was generated against the corresponding maps using PHENIX in real space with secondary structure and geometry restraints. The model stereochemistry was evaluated by the comprehensive validation (cryo-EM) tool in PHENIX.

All figures were prepared using open-source PyMOL[57] or UCSF Chimera[58].

[3H]Noradrenaline uptake assay
To perform the [3H]noradrenaline uptake assay, HEK293F cells were infected with P2 viruses (1:100) following protein expression protocol. After an 18-h incubation at 37 °C with 5% CO_2 in suspension at 125 rpm, 2×10^6 cells were harvested by centrifugation at 300g for 3 min. The cells were washed with 1 ml of warm PBSCM buffer (137 mM NaCl, 2.7 mM KCl, 4.3 mM Na_2HPO_4, 1.4 mM KH_2PO_4, 0.1 mM $CaCl_2$, and 0.5 mM $MgCl_2$, pH 7.4) in a 1.5-ml tube.

Transportation assays were conducted in 150 µl PBMCM buffer and nonspecific uptake was determined by including 100 µM of the potent noradrenaline transporter inhibitor, atomoxetine. To determine the initial transportation rates of NET[EM] and S2 site-related mutants, the reaction was initiated by adding 5 µM nonradioactive noradrenaline and 20 nM [3H]noradrenaline, followed by incubation for 3, 6 or 9 min. For the inhibition studies, cells were preincubated in PBSCM buffer containing the indicated concentrations of inhibitors for 15 min to achieve equilibrium. Due to the poor water solubility of ziprasidone, 2% DMSO was added to the PBSCM buffer. [3H]noradrenaline uptake was initiated by addition of 5 µM nonradioactive noradrenaline and 20 nM [3H]noradrenaline. To determine the K_m value of NET[WT] and NET[EM], reactions were initiated by adding a series of [3H]noradrenaline concentration (0.5 µM, 1 µM, 2 µM, 4 µM and 8 µM). Reactions were terminated by adding 1 ml of ice-cold PBSCM buffer, followed by centrifugation at

13,000 rpm for 15 s to collect cells. The cells were than lysed with 1% Triton for 5 min at room temperature and transferred to scintillation fluid. The radioactivity counts were measured using a Microbeta plate reader (PerkinElmer).

The IC$_{50}$ values were determined using nonlinear regression with the equation $y = \frac{100}{1 + 10^{x - \log(IC_{50})}}$ in GraphPad Prism 9. K_m values were calculated by fitting to the Michaelis–Menten equation.

Proteoliposome preparation and transport assay
The purified NET[EM] was reconstituted into liposome composed solely of brain polar lipids. Initially, brain polar lipids in chloroform were vacuum dried and resuspended in a buffer containing 25 mM HEPES, pH 7.5, and 200 mM KCl to 20 mg ml⁻¹. This mixture underwent 5× freeze–thaw cycles before being extruded through a 0.4-µm filter (Millipore) and destabilized by the addition of 0.5% Triton X-100. Subsequently, purified NET[EM] (0.2 mg ml⁻¹) was mixed with destabilized lipids in a 1:50 protein:lipid (wt/wt) ratio and incubated at 4 °C for 30 min under gentle rotation. Bio-Beads SM-2 (Bio-Rad Laboratories), equilibrated in 25 mM HEPES, pH 7.5, and 200 mM KCl, were added to a concentration of 40 mg ml⁻¹ and incubated at 4 °C for 30 min under gentle rotation. The same quantity of Bio-Beads was added after 30 min, 60 min, 120 min and 12 h. After the final addition, the liposomes and beads incubated for an additional 2 h, followed by filtration to remove Bio-Beads. The proteoliposome samples were harvested by centrifugation at 73,000g for 30 min. The pelleted proteoliposomes were resuspended to 2.5 mg ml⁻¹ lipid in an intra-vesicular buffer containing 25 mM HEPES, pH 7.5, 200 mM KCl and was subsequently extruded through a 0.4-µm filter (Millipore).

Uptake assays were performed in a 2 ml tube in a 28 °C metal bath. Nonspecific signals were measured using proteoliposomes incubated with 100 µM atomoxetine for 15 min prior to [3H]noradrenaline uptake. The total reaction volume is 150 µl. To initiate the uptake assay, the proteoliposomes were diluted to a final concentration of 0.5 mg ml⁻¹ lipid in the buffer containing 25 mM HEPES, pH 7.5, and 200 mM NaCl supplemented with [3H]noradrenaline. For the assay determining kinetics parameters, uptake was initiated by the addition of [3H]noradrenaline at concentrations ranged from 62.5 nM to 2 µM. The protein quantity was assessed based on the GFP fluorescent intensity observed in the SDS–PAGE analysis. The image was taken by Tanon 5200 Multi instrument (Tanon). Analysis of the band intensity was performed using ImageJ. For the inhibition assay, proteoliposomes were was initially incubated with the inhibitor for 15 min to obtain equilibrium (2% DMSO was added for ziprasidone experiment), and then the reaction was initiated by addition of 100 nM [3H]noradrenaline. The transportation duration for all the experiments was 15 min, falling within the range of initial rate kinetics. Subsequently, 2 ml ice-cold wash buffer containing 25 mM HEPES, pH 7.5, 200 mM KCl was added, followed by filter through a 0.22-µm filter. The filter was then washed by 4 ml ice-cold wash buffer and then socked with 5 ml scintillation fluid in a 20-ml counting tube. The radioactivity counts were measured using a Hidex 300 SL instrument (HIDEX). The K_m and V_{max} values was calculated by fitting to Michaelis–Menten equation. The IC$_{50}$ values were determined using nonlinear regression with the equation $y = \frac{100}{1 + 10^{x - \log(IC_{50})}}$ in GraphPad Prism 9.

Scintillation proximation assay
Competition binding experiments were conducted using a scintillation proximity assay. In brief, a mixture consisting of 20 nM NET nanodisc sample, 25 nM [3H]nisoxetine, 1 mg ml⁻¹ Cu-Ysi beads (PerkinElmer) and varying concentrations of cold competitors was thoroughly mixed for 1 h at 4 °C under gentle shaking in PBS buffer containing 0.2% BSA. For ziprasidone competition assay, the buffer also contained 2% DMSO to increase the solubility of ziprasidone. The signals were then counted using a Microbeta plate reader (PerkinElmer). Background signals were determined by the addition of 20 µM desipramine. Data points

Article

represent mean ± s.e.m. of three independent assays. K_i values were determined using the Cheng–Prusoff equation.

Reporting summary

Further information on research design is available in the Nature Portfolio Reporting Summary linked to this article.

Data availability

The three-dimensional cryo-EM density maps of the NET[Apo], NET[NA], NET[MrIA], NET[ZPD] and NET[BPP] have been deposited in the Electron Microscopy Data Bank under the accession codes EMD-37842, EMD-37843, EMD-37844, EMD-37845 and EMD-37846, respectively. The coordinates for NET[Apo], NET[NA], NET[MrIA], NET[ZPD] and NET[BPP] have been deposited in Protein Data Bank under accession codes 8WTU, 8WTV, 8WTW, 8WTX and 8WTY, respectively. Source data are provided with this paper.

51. Yu, R. et al. Enhanced activity against multidrug-resistant bacteria through coapplication of an analogue of tachyplesin I and an inhibitor of the QseC/B signaling pathway. *J. Med. Chem.* **63**, 3475–3484 (2020).
52. Zheng, S. Q. et al. MotionCor2: anisotropic correction of beam-induced motion for improved cryo-electron microscopy. *Nat. Methods* **14**, 331–332 (2017).
53. Zhang, K. Gctf: real-time CTF determination and correction. *J. Struct. Biol.* **193**, 1–12 (2016).
54. Punjani, A., Rubinstein, J. L., Fleet, D. J. & Brubaker, M. A. cryoSPARC: algorithms for rapid unsupervised cryo-EM structure determination. *Nat. Methods* **14**, 290–296 (2017).
55. Emsley, P., Lohkamp, B., Scott, W. G. & Cowtan, K. Features and development of Coot. *Acta Crystallogr. D* **66**, 486–501 (2010).
56. Adams, P. D. et al. PHENIX: a comprehensive Python-based system for macromolecular structure solution. *Acta Crystallogr. D* **66**, 213–221 (2010).
57. DeLano, W. L. Pymol: An open-source molecular graphics tool. *CCP4 Newsl. Protein Crystallogr.* **40**, 82–92 (2002).
58. Pettersen, E. F. et al. UCSF Chimera—a visualization system for exploratory research and analysis. *J. Comput. Chem.* **25**, 1605–1612 (2004).

Additional information

Extended Data Fig. 1 | Purification and functional characterization of NET. a-b, Gel-filtration profile of purified NET^{WT} (a) and NET^{EM} (b) in the presence of 0.025% (w/v) DDM plus 0.015% CHS. **c**, Concentration-dependence of norepinephrine uptake by NET^{WT} and NET^{EM}. Data represent mean ± SEM obtained from three biological experiments. There is no significant difference ($p = 0.4$) in K_m value for NET^{EM} ($0.32 ± 0.05\mu M$) and NET^{WT} ($0.24 ± 0.03\mu M$). **d-f**, Inhibition of [³H]NE uptake in NET^{EM} and NET^{WT} by χ-MrlA^{EM} (**d**), bupropion (**e**), and ziprasidone (**f**). Data represent mean ± SEM obtained from three biological experiments. t-test was employed to compare the IC_{50} values for χ-MrlA^{EM}, bupropion, and ziprasidone between NET^{EM} and NET^{WT}. The resulting p-values were 0.0916, 0.7056, and 0.0541, respectively, indicating that the differences were not statistically significant. **g**, Gel-filtration profile of NET^{EM} in nanodisc. **h**, Coomassie-blue-stained SDS-PAGE gel of NET^{EM} in nanodisc. For gel source data, see Supplementary Fig. 1. **i**, Concentration-dependence

of norepinephrine uptake of NET^{EM} in proteoliposome. The results were fitted to 'Michaelis Menten' equation, determining the K_m and V_{max} value of norepinephrine transport as $0.17 ± 0.08\,\mu M$ and 904.7 pmol/min/mg, respectively. **j-l**, Inhibition of [³H]NE uptake by χ-MrlA^{EM} (**j**), bupropion (**k**), and ziprasidone (**l**) on NET^{EM} in proteoliposome. The normalized data of inhibition assay were fitted using non-parametric nonlinear regression, yielding IC_{50} values of $113.5 ± 34.2$ nM for χ-MrlA^{EM}, $6.0 ± 3.1\,\mu M$ for bupropion and $259.4 ± 87.1$ nM for ziprasidone. **m-p**, Competition binding assays for nisoxetine (**m**), χ-MrlA^{EM} (**n**), bupropion (**o**), and ziprasidone (**p**) were performed to compete against [³H]nisoxetine using scintillation proximity assay. Data points represent mean ± SEM from three independent assays. The K_i values for nisoxetine, χ-MrlA^{EM}, bupropion, and ziprasidone are $21.9 ± 4.7$ nM, $144.3 ± 11.3$ nM, $13.1 ± 1.4\,\mu M$, and $163.7 ± 20.3$ nM, respectively.
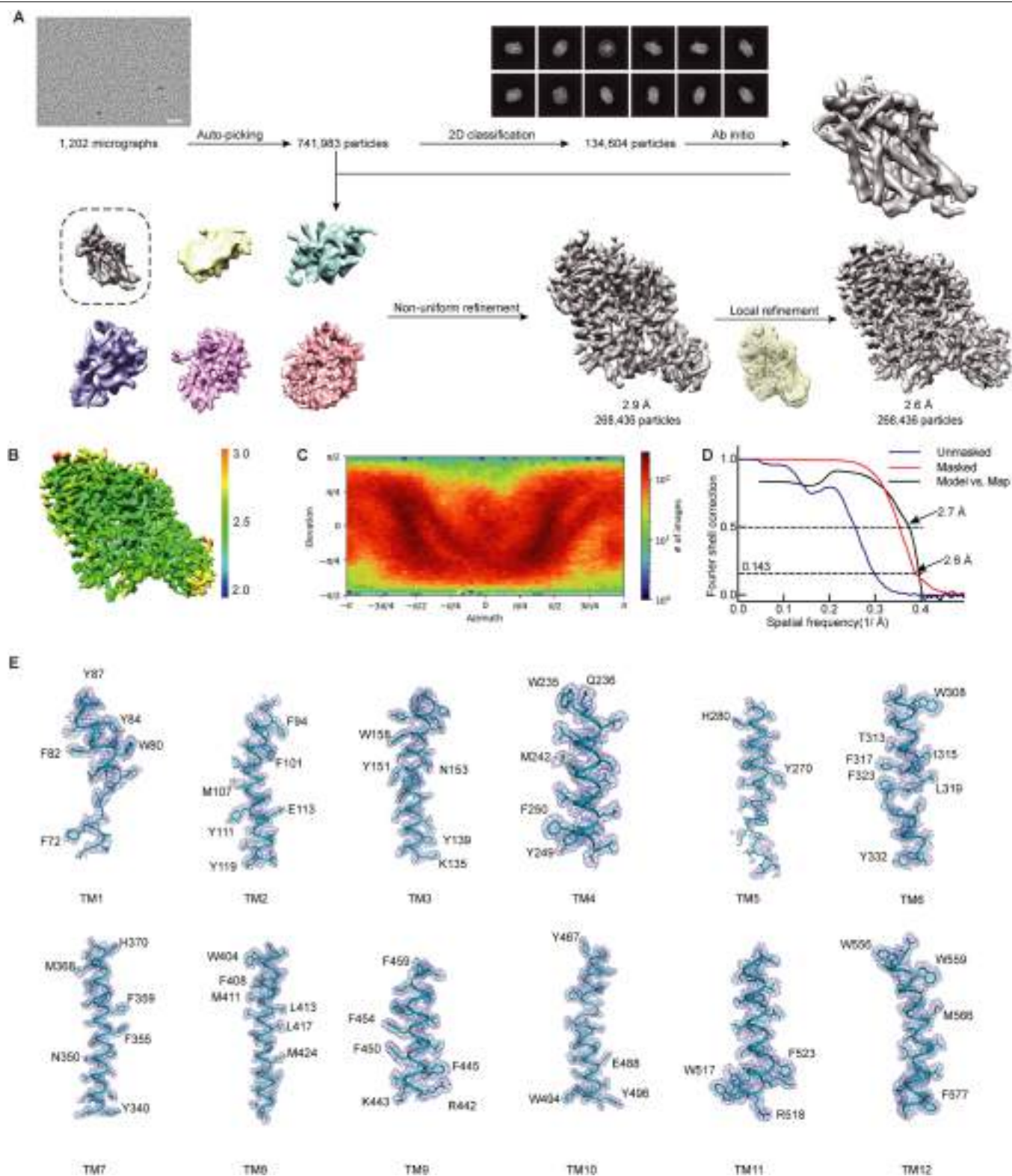
Extended Data Fig. 2 | Cryo-EM reconstruction of NET^Apo. a, Cryo-EM data processing workflow for NET^Apo in the inward-open conformation. A representative micrograph was shown with the white bar equals 100 nm. **b**, Local resolution map of NET^Apo, with colors representing local resolution estimates ranging from 2.0 to 3.0 Å. **c**, Angular sampling of the final reconstruction, illustrating the orientation distribution of particles in the final reconstruction of NET^NA. **d**, Map-map and map-model Fourier shell correlations (FSC) curves. **e**, Electron density visualization of transmembrane helices in the NET^Apo structure.
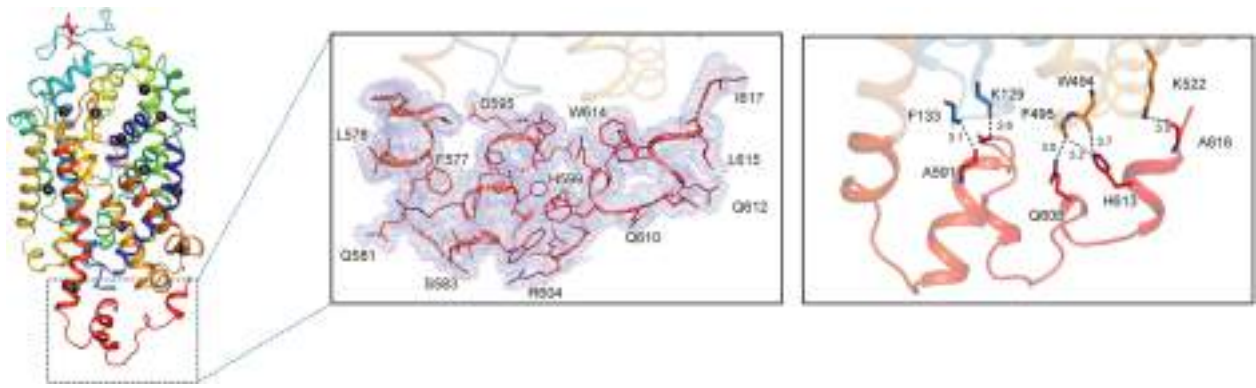
Extended Data Fig. 3 | C-terminus structure of NET. (left): The cartoon representation of the NET^{MrlA} structure is color-coded in a rainbow spectrum. (middle): Detailed view of c-terminus of NET. The electron density is depicted as a slate-colored mesh. Residues within the C-terminus are visualized as sticks. (right): Interaction network between c-terminus and core region of NET. Residues participating in these interactions are represented as sticks and labeled. Hydrogen bond interactions are represented as black dash lines, with distances labeled.
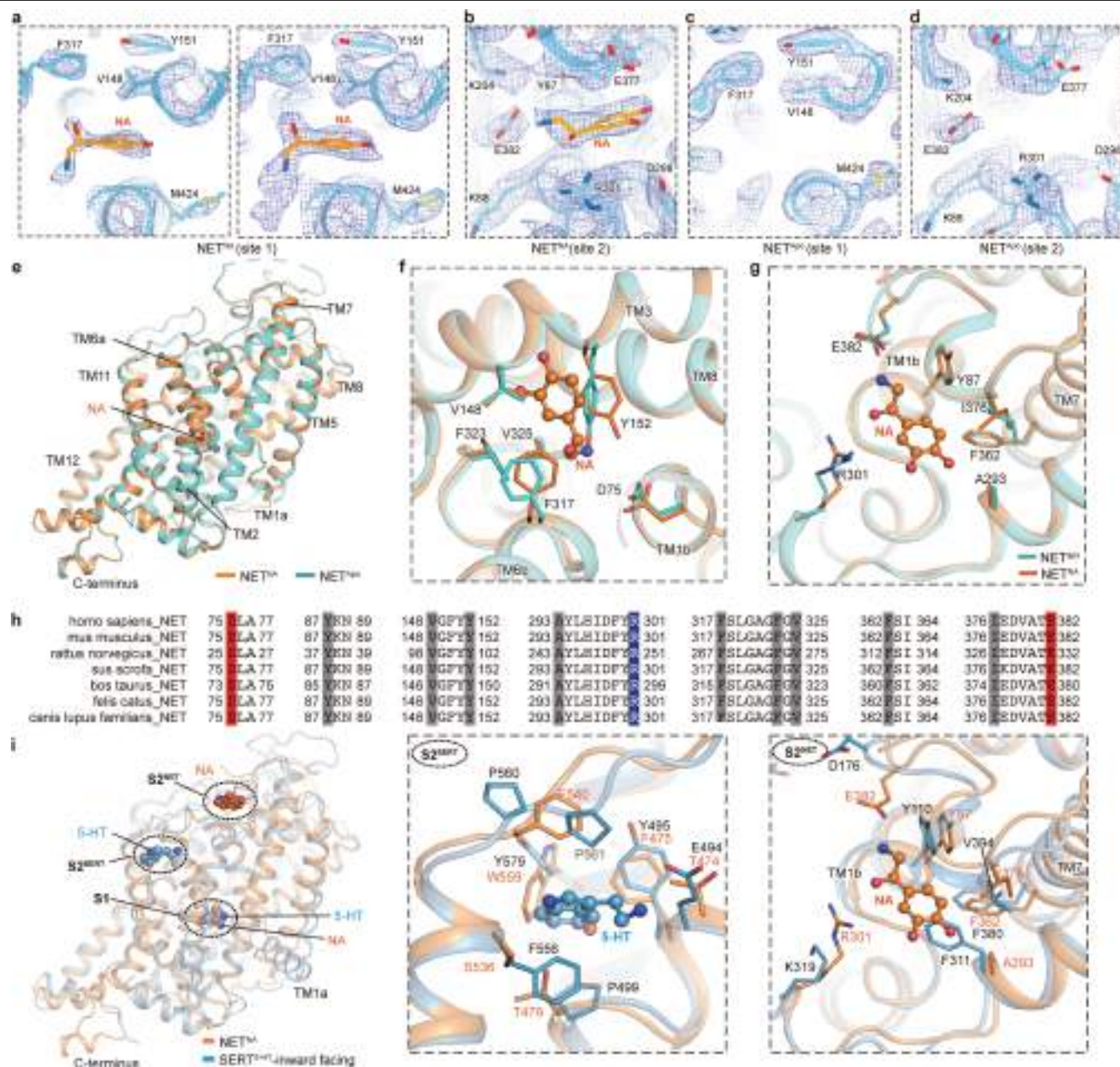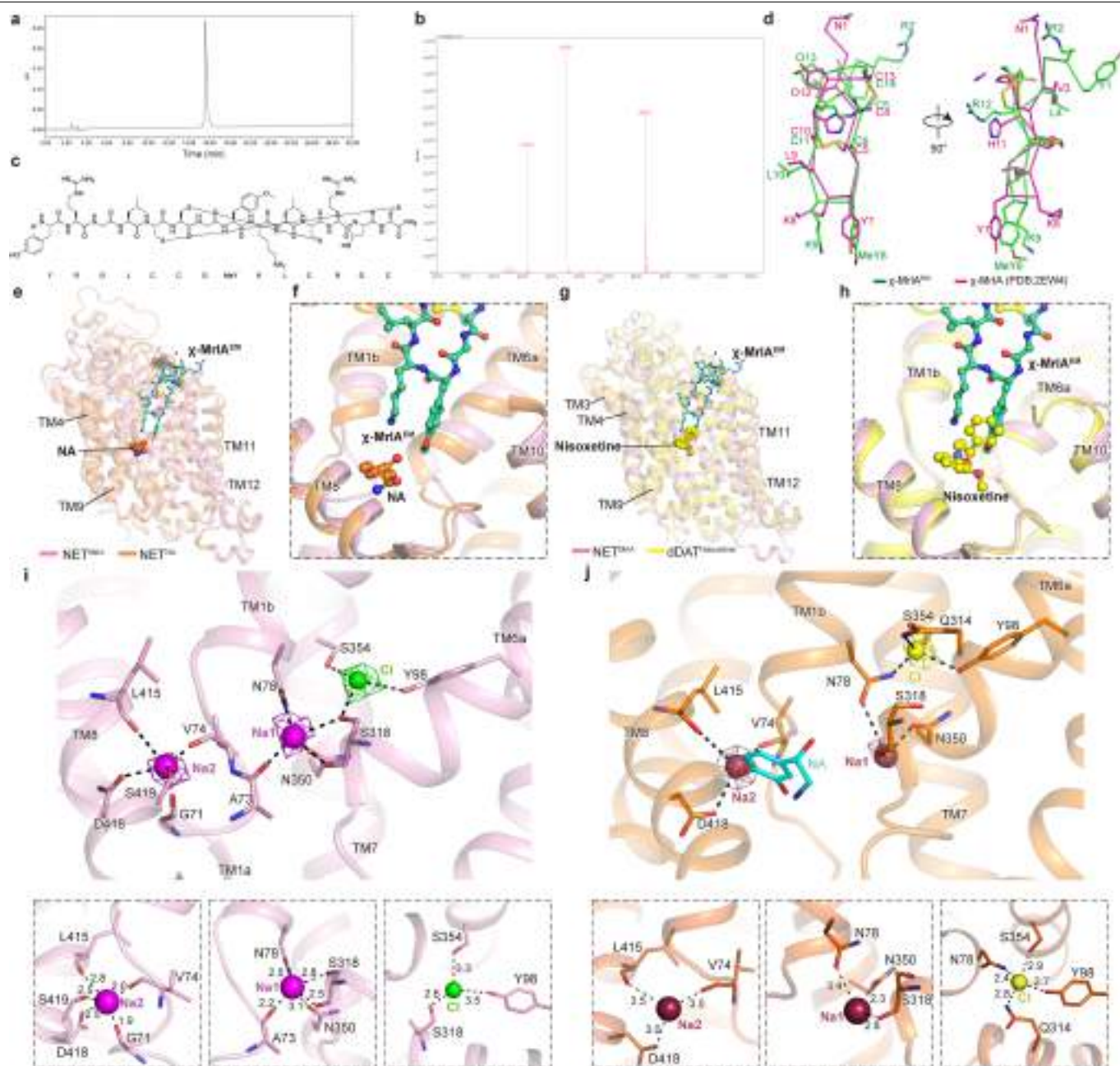
Extended Data Fig. 4 | Structural analysis of the norepinephrine binding sites. a-d, Cryo-EM density (blue mesh) corresponding to substrate norepinephrine at central binding site (**a/c**) and S2 binding site (**b/d**) in the NET[NA] structure and NET[Apo] structure, respectively. The density maps are showed in threshold countered at 1.0 (left in **a**), 0.6 (right in **a**), 0.8 (**b**), 0.6 (**c**) and 0.8 (**d**) in ChimeraX, respectively. NET[NA] is shown as cyan cartoon, and substrate NE is shown as orange sticks. **e**, Overall structural comparison of NET[Apo] (cyan) and NET[NA] (orange). **f**, Detailed comparison of S1 binding site between NET[NA] and NET[Apo]. Residues surrounding NA are shown as sticks. **g**, Detailed comparison of S2 binding site between NET[NA] and NET[Apo]. Residues surrounding NA are shown as sticks. **h**, The sequence alignment of NET from different species at key residues in the NE binding sites. **i**, Structural alignment with SERT (PDB: 7LI9) using overall structure. Superposition of NET (orange) onto SERT (skyblue) complexed with serotonin, both adopting the inward conformation. S2[SERT] and S2[NET]: Secondary binding sites specific to 5-HT and NA, respectively.
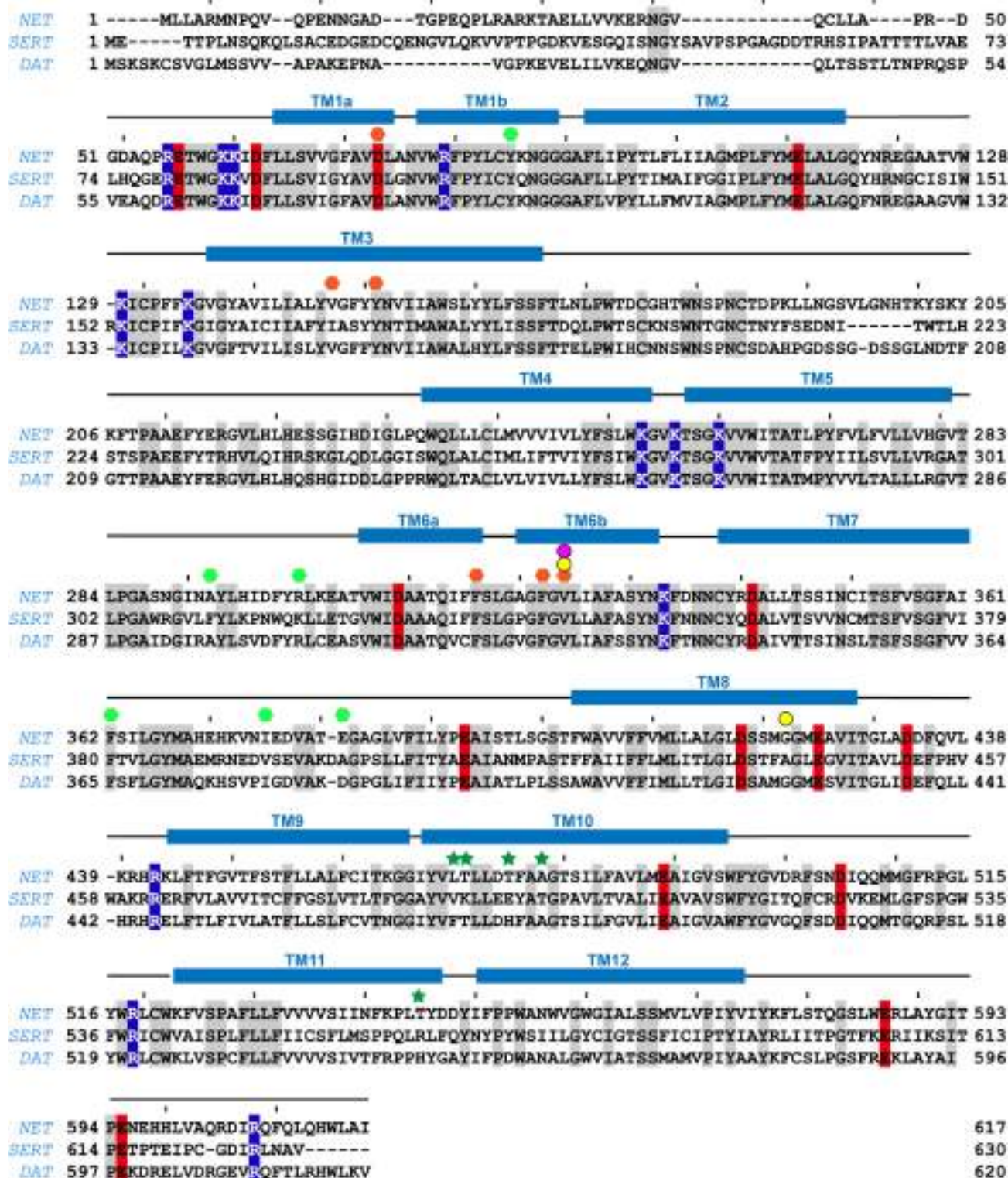
Extended Data Fig. 5 | Amino acid sequence of human monoamine transporter. Multiple sequence alignment analysis was conducted for monoamine transporters, incorporating human NET (Uniprot ID: P23975), SERT (Uniprot ID: P31645), and DAT (Uniprot ID: Q01959). Strictly conserved negatively and positively charged residues were respectively highlighted in red and blue, while other conserved residues were annotated in grey. Black bars above the sequence were employed to indicate every ten residues, including gaps. The transmembrane helices were labeled with blue strips. The orange and light green hexagon show residues involved in coordinating substrate in S1 and S2 substrate binding site, respectively. The green stars indicate residues involved in mutation studies of χ-MrIA. The yellow and magenta circles mark residues involved in mutation studies of bupropion and ziprasidone, respectively.

Extended Data Fig. 6 | Structural analysis of χ-MrlA^EM and ion binding sites.
a, HPLC chromatogram of MrlA^EM obtained using the Waters e2695 Separations Module and 2998 PDA Detector at 220 nm, the mobile phase employed a 30-minute gradient from 90% mobile phase A to 60% mobile phase A (mobile phase A: water with 0.05% TFA; mobile phase B: acetonitrile with 0.05% TFA). **b**, MS chromatogram of MrlA^EM using the Waters 2998 PDA Detector, the theoretical mass of MrlA^EM was 1660.03, and the observed mass-to-charge ratio (m/z) were as follows: 830.35[M + 2H]2 +, 553.97[M + 3H]3 +, 415.64[M + 4H]4 +. **c**, Chemical structure of MrlA^EM drawn by ChemBioDraw Ultra 14.0, the unnatural amino acid MeY and O represents O-methyl-L-tyrosine and L-trans-hydroxyproline, respectively. **d**, Superposition of χ-MrlA^EM (magenta) and χ-MrlA (PDB ID: 2EW4) (green) are based on the overall structure. The one-letter

code and position of the corresponding amino acids are labeled. MeY represents o-methyl-l-tyrosine. **e-f**, Superposition between NET^MrlA (pink) and NET^NA (orange) based on scaffold domain. The binding positions of χ-MrlA and NA do not overlap while χ-MrlA and NA are represented as green and orange sticks/spheres, respectively. **g-h**, Superposition between NET^MrlA (pink) and dDAT^Nisoxetine (PDB ID: 4XNU) (yellow) based on scaffold domain. The binding positions of χ-MrlA and Nisoxetine overlap while χ-MrlA and Nisoxetine are represented as green and purple sticks/spheres, respectively. **i**, Interaction network at the ionic binding site in the outward-open structure NET^MrlA. Sodium and chloride ions are represented by purple and green balls, respectively. **j**, Interaction network at the ionic binding site in the inward-open structure NET^NA. Sodium and chloride ions are represented by brown and yellow balls, respectively.
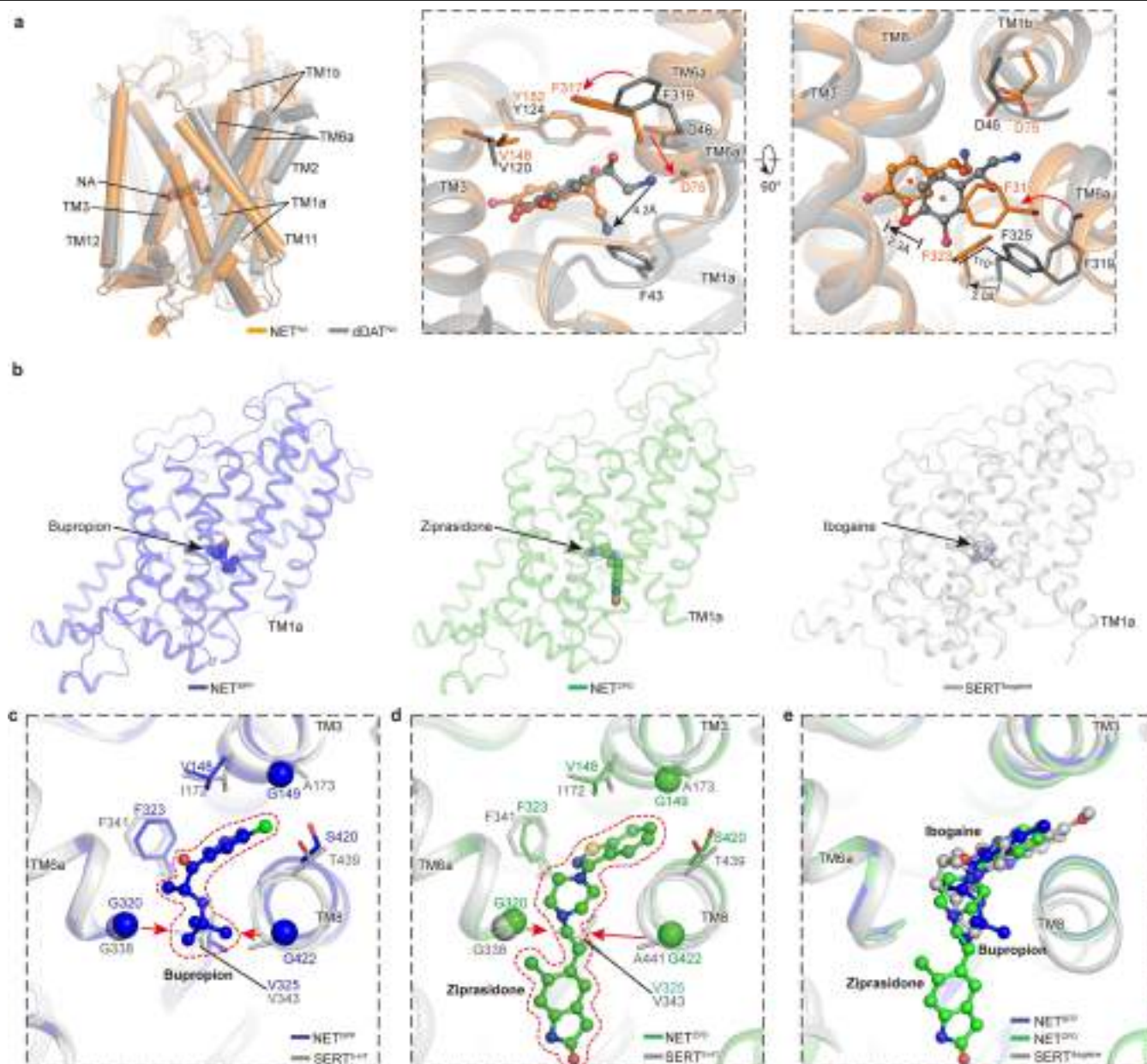
Extended Data Fig. 7 | Structural comparisons of substrate and inhibitor binding sites. a, The displacement of substrate NA during conformational transition from outward-facing to inward-facing state. Structural comparison of NET[NA] and dDAT[NA] (PDB: 6M0Z) are carried out using the scaffold domain as a reference. The structures of NET[NA] and dDAT[NE] are colored in orange and grey, respectively. (inset) Substrate NA molecules are shown as spheres and sticks. Key residues involved in substrate binding are represented as sticks. The displacement of substrate NA and side chains of key residues are labeled. **b**, Binding position comparison of bupropion, ziprasidone and ibogaine. The structures of NET[BPP] and NET[ZPD] are depicted as slate and green cartoon, respectively. The structure of SERT bound with ibogaine (SERT[ibogaine]) in inward-facing state (PDB ID: 6DZZ) is depicted as green cartoon. Ligands are represented as spheres. **c**, The binding mode of bupropion. Superposition was performed between NET[BPP] and SERT bound with serotonin (SERT[5-HT]) in inward-facing state (PDB ID: 7LI9) based on the overall structure. NET[BPP] and SERT[5-HT] are colored in blue and grey, respectively. Residues surrounding the binding site are visualized as sticks. **d**, The binding mode of ziprasidone. Superposition was carried out between NET[ZPD] and SERT[5-HT] in the inward-open conformation based on the overall structure. NET[ZPD] and SERT[5-HT] are colored in green and grey, respectively. Residues surrounding the binding site are visualized as sticks. **e**, A comparative analysis of the binding modes of bupropion, ziprasidone, and ibogaine is provided, highlighting their differences of binding positions.

Extended Data Fig. 8 | The working and inhibitory mechanism of NET.
Key helices involved in the conformational changes are colored and labeled,
whereas the scaffold domain and C-terminus are depicted in gray. The
intracellular and extracellular cavities are represented by purple shadows.
Molecules of noradrenaline, nisoxetine, bupropion, and ziprasidone molecules
are depicted as spheres, while χ-conotoxin MrIA is shown as a green cartoon
and surface.

Extended Data Table 1 | Assessment of transport properties and the inhibitory effects of drugs on NET

Ligand	NET^{WT} (Intact cells)	NET^{EM} (Intact cells)	NET^{EM} (Brain polar lipid proteoliposome)
Noradrenaline (K_m)	0.24 ± 0.03 μM	0.32 ± 0.05 μM	0.17 ± 0.08 μM
χ-MrlA^{EM} (IC_{50})	103.9 ± 2.00 nM	139.5 ± 1.28 nM	113.5 ± 34.2 nM
Bupropion (IC_{50})	14.1 ± 2.80 μM	14.8 ± 1.30 μM	6.0 ± 3.10 μM
Ziprasidone (IC_{50})	309.3 ± 75.8 nM	525.0 ± 9.20 nM	259.4 ± 87.1 nM

Transport assays were conducted in both HEK293 cells and proteoliposomes reconstituted with brain polar lipids. Data represent mean±SEM obtained from three independent biological experiments.

Article

Extended Data Table 2 | Cryo-EM data collection, refinement and validation statistics

	NET^{Apo} (EMD-37842) (PDB 8WTU)	NET^{NA} (EMD-37843) (PDB 8WTV)	NET^{MrlA} (EMD-37844) (PDB 8WTW)	NET^{BPP} (EMD-37845) (PDB 8WTX)	NET^{ZPD} (EMD-37846) (PDB 8WTY)
Data collection and processing					
Magnification	×105,000	×105,000	×105,000	×105,000	×105,000
Voltage (kV)	300	300	300	300	300
Electron exposure (e⁻/Å²)	60	60	60	60	60
Defocus range (µm)	−1.2 − −2.2	−1.2 − −2.2	−1.2 − −2.2	−1.2 − −2.2	−1.2 − −2.2
Pixel size (Å)	0.85	0.85	0.85	0.85	0.85
Symmetry imposed	C1	C1	C1	C1	C1
Initial particle images (no.)	741,983	2,321,152	2,041,165	2,009,739	1,117,052
Final particle images (no.)	268,436	361,801	313,089	584,926	375,649
Map resolution (Å)	2.6	2.6	2.8	2.8	3.2
FSC threshold	0.143	0.143	0.143	0.143	0.143
Refinement					
Model resolution (Å)	2.7	2.7	3.0	2.9	3.4
FSC threshold	0.5	0.5	0.5	0.5	0.5
Map sharpening B factor (Å²)	-103.2	-97.6	-125.0	-131.0	-157.3
Model composition					
Non-hydrogen atoms	4348	4311	4531	4300	4345
Protein residues	542	538	564	536	540
Ligands	1	6	5	1	1
B factors (Å²)					
Protein	35.17	33.02	49.95	42.88	20.42
Ligand	56.50	53.22	53.85	57.80	29.47
R.m.s. deviations					
Bond lengths (Å)	0.003	0.002	0.002	0.003	0.002
Bond angles (°)	0.674	0.475	0.430	0.654	0.536
Validation					
MolProbity score	1.21	0.99	1.19	1.50	1.48
Clashscore	2.00	2.00	4.00	5.00	3.00
Poor rotamers (%)	0.20	0.90	0.60	0.70	0.40
Ramachandran plot					
Favored (%)	96.00	98.00	98.00	95.00	94.00
Allowed (%)	4.00	2.00	2.00	5.00	6.00
Disallowed (%)	0.00	0.00	0.00	0.00	0.00

Data collection, refinement and validation statistics for human NET^{Apo}, NET^{NA}, NET^{MrlA}, NET^{BPP}, and NET^{ZPD} complexes.

Corresponding author(s): Yan Zhao

Last updated by author(s): May 16, 2024

Reporting Summary

Nature Portfolio wishes to improve the reproducibility of the work that we publish. This form provides structure for consistency and transparency in reporting. For further information on Nature Portfolio policies, see our Editorial Policies and the Editorial Policy Checklist.

Statistics

For all statistical analyses, confirm that the following items are present in the figure legend, table legend, main text, or Methods section.

n/a	Confirmed	
☐	☒	The exact sample size (*n*) for each experimental group/condition, given as a discrete number and unit of measurement
☐	☒	A statement on whether measurements were taken from distinct samples or whether the same sample was measured repeatedly
☐	☒	The statistical test(s) used AND whether they are one- or two-sided *Only common tests should be described solely by name; describe more complex techniques in the Methods section.*
☒	☐	A description of all covariates tested
☒	☐	A description of any assumptions or corrections, such as tests of normality and adjustment for multiple comparisons
☐	☒	A full description of the statistical parameters including central tendency (e.g. means) or other basic estimates (e.g. regression coefficient) AND variation (e.g. standard deviation) or associated estimates of uncertainty (e.g. confidence intervals)
☐	☒	For null hypothesis testing, the test statistic (e.g. *F*, *t*, *r*) with confidence intervals, effect sizes, degrees of freedom and *P* value noted *Give P values as exact values whenever suitable.*
☒	☐	For Bayesian analysis, information on the choice of priors and Markov chain Monte Carlo settings
☒	☐	For hierarchical and complex designs, identification of the appropriate level for tests and full reporting of outcomes
☒	☐	Estimates of effect sizes (e.g. Cohen's *d*, Pearson's *r*), indicating how they were calculated

Our web collection on statistics for biologists contains articles on many of the points above.

Software and code

Policy information about availability of computer code

Data collection	EPU Version 2.14.0.3653REL
Data analysis	Gctf 1.18, cryoSPARC 3.0, Pymol 2.5, UCSF chimeraX 1.11, Coot 0.9.2-pre, PHENIX 1.18.2, GraphPad Prism 9

For manuscripts utilizing custom algorithms or software that are central to the research but not yet described in published literature, software must be made available to editors and reviewers. We strongly encourage code deposition in a community repository (e.g. GitHub). See the Nature Portfolio guidelines for submitting code & software for further information.

Data

Policy information about availability of data

All manuscripts must include a data availability statement. This statement should provide the following information, where applicable:
- Accession codes, unique identifiers, or web links for publicly available datasets
- A description of any restrictions on data availability
- For clinical datasets or third party data, please ensure that the statement adheres to our policy

All accession codes including UniProtKB, PDB AND EMDB IDs will be updated in the following revisions.

Research involving human participants, their data, or biological material

Policy information about studies with [human participants or human data](#). See also policy information about [sex, gender (identity/presentation), and sexual orientation](#) and [race, ethnicity and racism](#).

Reporting on sex and gender	*Use the terms sex (biological attribute) and gender (shaped by social and cultural circumstances) carefully in order to avoid confusing both terms. Indicate if findings apply to only one sex or gender; describe whether sex and gender were considered in study design; whether sex and/or gender was determined based on self-reporting or assigned and methods used.* *Provide in the source data disaggregated sex and gender data, where this information has been collected, and if consent has been obtained for sharing of individual-level data; provide overall numbers in this Reporting Summary. Please state if this information has not been collected.* *Report sex- and gender-based analyses where performed, justify reasons for lack of sex- and gender-based analysis.*
Reporting on race, ethnicity, or other socially relevant groupings	*Please specify the socially constructed or socially relevant categorization variable(s) used in your manuscript and explain why they were used. Please note that such variables should not be used as proxies for other socially constructed/relevant variables (for example, race or ethnicity should not be used as a proxy for socioeconomic status).* *Provide clear definitions of the relevant terms used, how they were provided (by the participants/respondents, the researchers, or third parties), and the method(s) used to classify people into the different categories (e.g. self-report, census or administrative data, social media data, etc.)* *Please provide details about how you controlled for confounding variables in your analyses.*
Population characteristics	*Describe the covariate-relevant population characteristics of the human research participants (e.g. age, genotypic information, past and current diagnosis and treatment categories). If you filled out the behavioural & social sciences study design questions and have nothing to add here, write "See above."*
Recruitment	*Describe how participants were recruited. Outline any potential self-selection bias or other biases that may be present and how these are likely to impact results.*
Ethics oversight	*Identify the organization(s) that approved the study protocol.*

Note that full information on the approval of the study protocol must also be provided in the manuscript.

Field-specific reporting

Please select the one below that is the best fit for your research. If you are not sure, read the appropriate sections before making your selection.

☒ Life sciences ☐ Behavioural & social sciences ☐ Ecological, evolutionary & environmental sciences

For a reference copy of the document with all sections, see [nature.com/documents/nr-reporting-summary-flat.pdf](#)

Life sciences study design

All studies must disclose on these points even when the disclosure is negative.

Sample size	Sample size were not predetermined for this study. The amount of micrographs is determined by the microscope time.
Data exclusions	No data was excluded from the analyses.
Replication	Cryo-EM sample preparation including purification, SDS-PAGE gels were reproduced at least three times independently. Transportation assay were repeated three times independently.
Randomization	Sample purification were repeated at least three times with different batches of cells.
Blinding	The investigators were not blinded as the parameter for cryo-EM analysis experiments did not require subjective assessments.

Reporting for specific materials, systems and methods

We require information from authors about some types of materials, experimental systems and methods used in many studies. Here, indicate whether each material, system or method listed is relevant to your study. If you are not sure if a list item applies to your research, read the appropriate section before selecting a response.

Materials & experimental systems

n/a	Involved in the study
☒	☐ Antibodies
☐	☒ Eukaryotic cell lines
☒	☐ Palaeontology and archaeology
☒	☐ Animals and other organisms
☒	☐ Clinical data
☒	☐ Dual use research of concern
☒	☐ Plants

Methods

n/a	Involved in the study
☒	☐ ChIP-seq
☒	☐ Flow cytometry
☒	☐ MRI-based neuroimaging

Eukaryotic cell lines

Policy information about cell lines and Sex and Gender in Research

Cell line source(s)	FreeStyle 293-F cells (gibco, USA);
Authentication	Not authentification
Mycoplasma contamination	The cells were tested negative for mycoplasma contamination.
Commonly misidentified lines (See ICLAC register)	Not commonly misidentified lines were used.

Plants

Seed stocks	*Report on the source of all seed stocks or other plant material used. If applicable, state the seed stock centre and catalogue number. If plant specimens were collected from the field, describe the collection location, date and sampling procedures.*
Novel plant genotypes	*Describe the methods by which all novel plant genotypes were produced. This includes those generated by transgenic approaches, gene editing, chemical/radiation-based mutagenesis and hybridization. For transgenic lines, describe the transformation method, the number of independent lines analyzed and the generation upon which experiments were performed. For gene-edited lines, describe the editor used, the endogenous sequence targeted for editing, the targeting guide RNA sequence (if applicable) and how the editor was applied.*
Authentication	*Describe any authentication procedures for each seed stock used or novel genotype generated. Describe any experiments used to assess the effect of a mutation and, where applicable, how potential secondary effects (e.g. second site T-DNA insertions, mosiacism, off-target gene editing) were examined.*